# SANDIA REPORT

SAND2018-1898
Unlimited Release
January 2018

# WSEAT Shock Testing Margin Assessment Using Energy Spectra Final Report

Carl Sisemore, Vit Babuška, Jason Booher

Prepared by
Sandia National Laboratories
Albuquerque, New Mexico 87185 and Livermore, California 94550

Sandia National Laboratories is a multimission laboratory managed and operated by National Technology and Engineering Solutions of Sandia, LLC., a wholly owned subsidiary of Honeywell International, Inc., for the U.S. Department of Energy's National Nuclear Security Administration under contract DE-NA0003525.

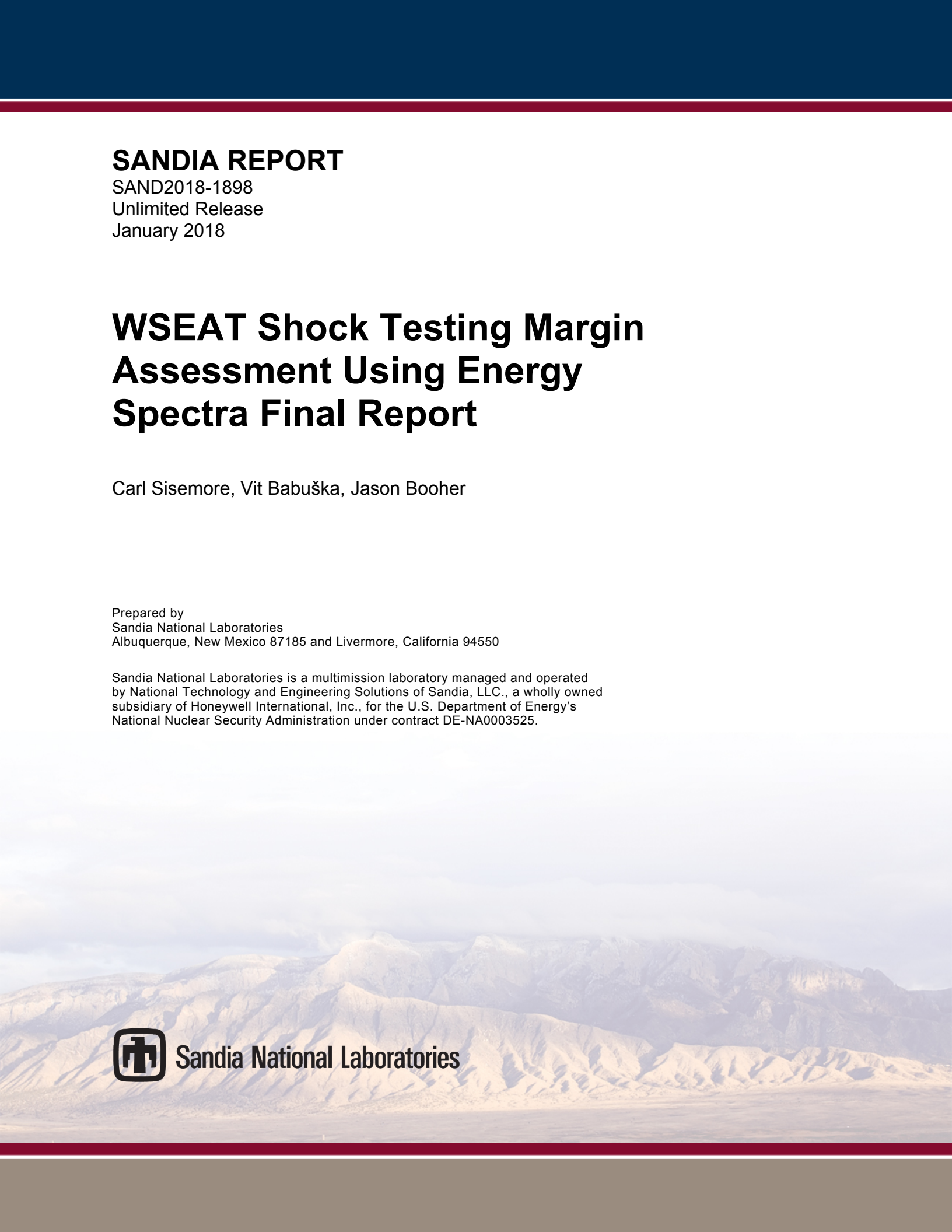

Issued by Sandia National Laboratories, operated for the United States Department of Energy by National Technology and Engineering Solutions of Sandia, LLC.

**NOTICE:** This report was prepared as an account of work sponsored by an agency of the United States Government. Neither the United States Government, nor any agency thereof, nor any of their employees, nor any of their contractors, subcontractors, or their employees, make any warranty, express or implied, or assume any legal liability or responsibility for the accuracy, completeness, or usefulness of any information, apparatus, product, or process disclosed, or represent that its use would not infringe privately owned rights. Reference herein to any specific commercial product, process, or service by trade name, trademark, manufacturer, or otherwise, does not necessarily constitute or imply its endorsement, recommendation, or favoring by the United States Government, any agency thereof, or any of their contractors or subcontractors. The views and opinions expressed herein do not necessarily state or reflect those of the United States Government, any agency thereof, or any of their contractors.

Printed in the United States of America. This report has been reproduced directly from the best available copy.

Available to DOE and DOE contractors from
U.S. Department of Energy
Office of Scientific and Technical Information
P.O. Box 62
Oak Ridge, TN 37831

Telephone: (865) 576-8401
Facsimile: (865) 576-5728
E-Mail: reports@osti.gov
Online ordering: http://www.osti.gov/scitech

Available to the public from
U.S. Department of Commerce
National Technical Information Service
5301 Shawnee Rd
Alexandria, VA 22312

Telephone: (800) 553-6847
Facsimile: (703) 605-6900
E-Mail: orders@ntis.gov
Online order: https://classic.ntis.gov/help/order-methods/

SAND2018-1898
Unlimited Release
January 2018

# WSEAT Shock Testing Margin Assessment Using Energy Spectra Final Report

Carl Sisemore, Vit Babuška, Jason Booher
Environments Engineering and Integration
Sandia National Laboratories
P.O. Box 5800
Albuquerque, New Mexico 87185-MS0840

**Abstract**

Several programs at Sandia National Laboratories have adopted energy spectra as a metric to relate the severity of mechanical insults to structural capacity. The purpose being to gain insight into the system's capability, reliability, and to quantify the ultimate margin between the normal operating envelope and the likely system failure point—a system margin assessment. The fundamental concern with the use of energy metrics was that the applicability domain and implementation details were not completely defined for many problems of interest. The goal of this WSEAT project was to examine that domain of applicability and work out the necessary implementation details.

The goal of this project was to provide experimental validation for the energy spectra based methods in the context of margin assessment as they relate to shock environments. The extensive test results concluded that failure predictions using energy methods did not agree with failure predictions using *S-N* data. As a result, a modification to the energy methods was developed following the form of Basquin's equation to incorporate the power law exponent for fatigue damage. This update to the energy-based framework brings the energy based metrics into agreement with experimental data and historical *S-N* data.

# ACKNOWLEDGMENTS

The authors would like to thank Mrs. Kim Haulenbeek for performing tensile coupon testing of the 3-D printed cantilever beam material and Mr. Dave Johnson for taking micrographs of the broken test specimen.

The authors would like to thank Mr. Matt Spletzer, Mr. Peter Renslow, Mr. D.J. Kenney, Mr. Randy Everett, and Mr. Gary Groves from the Mechanical Shock Laboratory for their help in performing the drop table testing on the cantilever beams.

The authors would like to thank Mr. Kevin Cross, Mr. Mark Halliburton, and Mr. Curt Tenorio from the Tech Area III Vibration Laboratory for their help performing the 6-DOF shaker shock experiments on the cantilever beams.

Several summer student interns also assisted with various aspects of this project and their assistance is greatly appreciated. Mr. Jack Reid, Mr. Dylan Murphy, and Mr. Darrius Stamps.

# TABLE OF CONTENTS

## FIGURES

## TABLES

# NOMENCLATURE

| | |
|---|---|
| ABS | Acrylonitrile Butadiene Styrene |
| CDL | Component Dynamics Laboratory |
| dB | decibel |
| DOE | Department of Energy |
| ERS | Energy Response Spectra |
| ISO | International Organization for Standardization |
| MMAA | Maxi-Max Absolute Acceleration |
| PCB | Printed Circuit Board |
| PVSRS | Pseudo-Velocity Shock Response Spectrum |
| RVSRS | Relative Velocity Shock Response Spectrum |
| SNL | Sandia National Laboratories |
| SRS | Shock Response Spectrum |
| WSEAT | Weapons Systems Engineering Assessment Technology |

# 1. INTRODUCTION

The Shock Response Spectrum (SRS) is the standard method for defining mechanical shock events. The idea behind the SRS is that all time histories with the same SRS will have essentially the same damage potential. The criticism of the SRS is that since it is a non-unique transform, there are theoretically an infinite number of time histories that can yield the same SRS. One alternative to the SRS is the energy spectrum. Energy spectra metrics for the analysis of shock data are nearly as old as the SRS. Hudson [1] and Housner [2] are generally credited with proposing the use of energy quantities to characterize transient base excitations resulting from earthquakes. Further analytical developments were published by Zahrah and Hall [3, 4] in the derivation of various energy terms with a focus on earthquake shock. More recently Edwards presented a framework using energy methods for shock analysis in aerospace applications [5].

Recently, several programs at Sandia National Laboratories have adopted energy spectra as a metric to relate the severity of mechanical insults to structural capacity. The purpose of this metric is to gain insight into the system's capability, reliability, and to quantify the ultimate margin between the normal operating envelope and the likely system failure point—a system margin assessment. A true system margin assessment is only possible if some units are destructively tested. By performing destructive testing, a measure of the damage necessary to fail a component can be determined. This can then be related to the damage potential of a subsequent event on a new or used component and a measure of the remaining life in a component can be determined.

One of the fundamental concerns with the use of energy metrics is that the applicability domain and implementation details have not been completely defined for many problems of interest. Specifically, energy dissipation models are not well defined and energy dissipation is generally assumed to be a function of constant modal damping. The specific failure criteria are also not well defined since most failures are localized failures as opposed to global failures. Most programs are concerned with functional failures of their equipment which may not necessarily be related to a gross structural failure. Many times, a functional failure can be induced by tripping a circuit breaker or cracking a solder joint while the structure remains completely intact.

The purpose of this investigation was to build a series of simple structures, test them to failure, and compare the failures seen with various damage metrics based on energy spectra. The goal of this study was to examine both first passage failures and low-cycle fatigue failures. One of the fundamental benefits often espoused about the energy metrics are their ability to consider cumulative damage from multiple insults [5]. Therefore, a simple study of repetitive shock to failure, or low cycle fatigue, seemed very appropriate to this research.

## 1.1. Overview of the Shock Response Spectrum

SRS are used from design and analysis of environment responses to defining specifications for laboratory testing. Use of the SRS has been described and codified in many publications, including Military and NASA standards. Since its introduction in the 1930s, the SRS has become ubiquitous because it has been shown to be an adequate and relatively simple

representation of a shock environment; in short it is useful for many structural issues involving shock loads.

A response spectrum transforms a transient excitation (i.e., a shock pulse) into a frequency domain representation of the response of a series of single degree of freedom oscillators, parameterized by natural frequency and damping ratio. This is shown in Figure 1 for a simple haversine base excitation. The most common SRS at SNL/NM is the maxi-max absolute acceleration (MMAA) SRS in which the excitation is a base acceleration and the response quantity is the maximum absolute value of the absolute acceleration over all time.

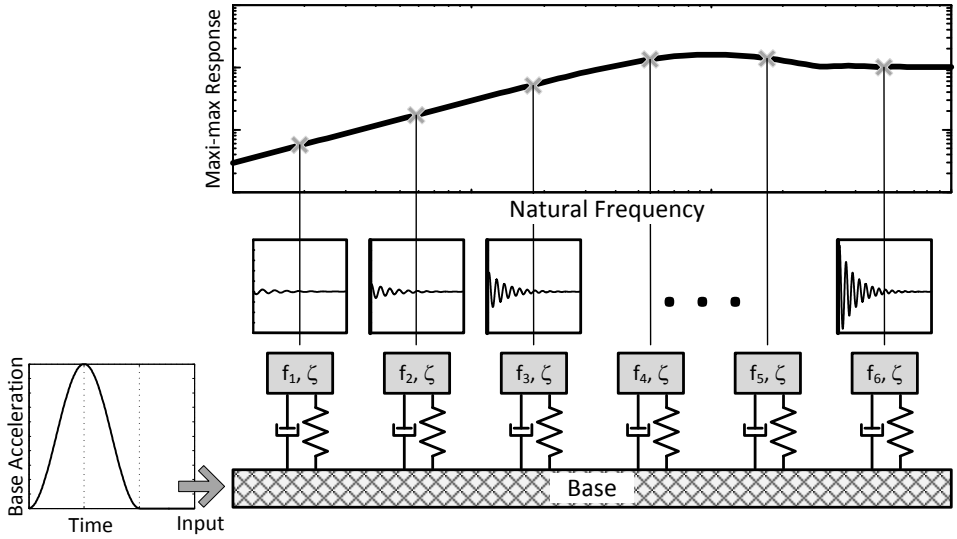


**Figure 1. Shock Response Spectrum Concept**

The SRS has many uses, including designing components to withstand shock loads. The general design methodology is shown in Figure 2. A transient excitation is transmitted through the primary structure to the base of the component of interest; for example, an electronics box. The SRS of the component base acceleration is computed. This greatly simplifies subsequent calculations and design iterations because transient analyses, which can be computationally expensive, are only done once. Assuming the component's modes are well separated, points on the SRS can be interpreted as unweighted maxi-max modal responses. Multiplying the SRS values at the component's modal frequencies by the corresponding modal gains and combining these products gives a quasi-static acceleration scalar that can be used for the design of components such as electronics boxes. References [6] and [7] discuss how MMAA SRS are used to design and analyze structures for shock environments.

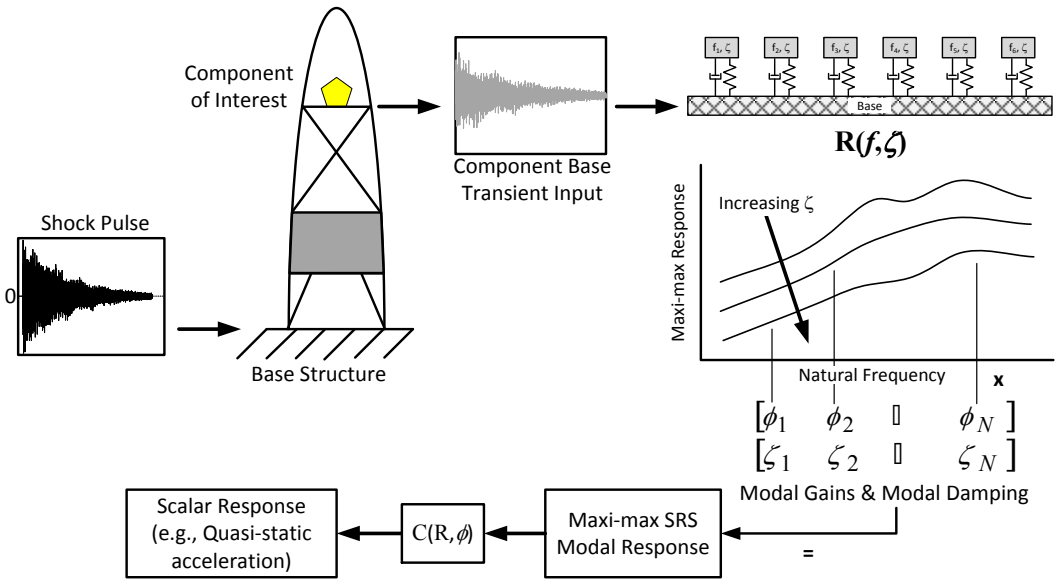


**Figure 2. The Shock Response Spectrum for Design**

SRS also are used to design test environments. A basic premise behind the SRS is that all time histories with the same SRS should have approximately the same shock damage potential. Strictly speaking, this is true only for single degree of freedom (SDOF) systems, but it has been shown to be generally true for multi-degree of freedom systems, where modal coupling can amplify the peak response. This makes an SRS very convenient for characterizing environments and translating them into equivalent test specifications. This property—that all time histories with the same SRS have the same shock damage potential—is a dangerous thing because one can be fooled into making physically meaningless time histories from an SRS. The SRS should not be used by itself when translating shock environments; other information such as temporal moments or event duration should be incorporated when synthesizing a time history.

The naval industry uses the Pseudo-Velocity Shock Response Spectrum (PVSRS) [8, 9], which is the product of relative displacement and frequency, rather than an acceleration SRS. The PVSRS has the advantage that the quantity from which the SRS is derived, relative displacement, is directly related to stress and strain. The PVSRS is often used as a measure of the damage potential of a shock.

Most components are designed to withstand a single shock. However, most systems are subjected to many shocks during their lifetime. Transportation environments expose a system to many low-level shock events. Spacecraft component shock qualification criteria impose up to 18 shocks (six in each axis) to verify that a component will withstand the one, or perhaps two shocks, it will experience during the launch phase of its life. This means that a qualification level shock environment is not the ultimate environment in which failure occurs from a single shock. These observations raise the questions:

- How much margin is available above the qualification shock environment?
- How many low-level shocks can a structure that was designed to withstand a single, high-intensity shock, absorb before suffering debilitating functional or structural damage?

The relationship between the damage potential of a series of relatively low-level shocks and a single high-level shock is complex and depends on many factors including the characteristics of the shock and failure mode of the component. Acceleration SRS and pseudo-velocity SRS are only applicable to single shocks in which the failure mode is overstress. Energy quantities seem better suited to capturing the effects of multiple shocks, because damage potential is a function of the way a structure distributes and dissipates the energy imparted to it.

## 1.2. Overview of Energy Response Spectrum

Energy response spectra were first proposed in the 1950's in the Civil Engineering community. Hudson [1] derived energy response spectra in terms of velocity response spectra. The derivation presented by Hudson stated that the absorbed energy spectra is half the square of the pseudo-velocity shock response spectra. As a result, the absorbed energy spectra contain the same information as a traditional pseudo-velocity shock response spectra.

The civil engineering community, specifically the seismic community, has long used energy based methods, including Energy Response Spectra (ERS) for describing the damage potential to structures from earthquakes [2, 3, 10], and energy based approaches continue to be addressed in current research. The foundation for the energy approach is that the failure mode of interest is structural failure, or loss of structural integrity. Structural failure is largely caused by large deformations dominated by the lowest resonant modes of a structure. Energy Response Spectra are analogs to SRS, but they are based on quantities more directly related to failure mechanisms of interest such as potential energy, kinetic energy, and total energy.

In aerospace applications, the failure modes are often subtler and more complex than earthquake failure modes. For example, failure of an electronic component in a shock environment is more common than a structural failure of a spacecraft. Shock induced mechanism trips, in which there is no structural failure, can doom a satellite or launch vehicle, turning it into space junk or a marine experiment. Examples of such failures are included in References [11] and [12]. If the shock sensitive component is relatively simple, for example a printed circuit board (PCB) in a chassis, the response to a shock at the component base may be dominated by the fundamental resonant mode. For larger, more dynamically complex parts, modal energy associated with failure of a shock sensitive part can be relatively small, so energy based methods borrowed directly from the civil engineering industry may not work as well. Energy spectra for multi-degree of freedom systems are discussed in Reference [13].

The difference between the civil engineering approach and the aerospace engineering approach is best described as the civil engineer wants to understand whether the building will remain standing during an earthquake whereas the aerospace engineer wants to know which window in the building might crack during an earthquake. It is simply a different scale for the problem.

# 2. RESPONSE SPECTRUM THEORY

All response spectra, MMAA SRS, PVSRS and ERS, are derived from the equation of motion of a single degree of freedom system subjected to a base excitation as shown in Figure 3. The equation of motion is given as:

$$m\ddot{x}(t) + c(\dot{y}(t) - \dot{x}(t)) + k(y(t) - x(t)) = 0 \tag{1}$$

This is the equation of motion for the absolute motion of the mass relative to an inertial reference frame. The equation of motion for the relative displacement is:

$$m\ddot{z}(t) + c\dot{z}(t) + kz(t) = -m\ddot{x}(t) \tag{2}$$

where $z(t) = y(t) - x(t)$ and is the relative displacement of the mass to the base. Dividing by $m$ gives

$$\ddot{z}(t) + 2\zeta\omega_n\dot{z}(t) + \omega_n^2 z(t) = -\ddot{x}(t) \tag{3}$$

In the above equation, the usual substitutions, $2\zeta\omega_n = c/m$ and $\omega_n^2 = k/m$, were made. The initial conditions at $t = 0$ are $z(0) = z_0$ and $\dot{z}(0) = \dot{z}_0$. The equation of motion is always paired with an output equation that defines the response quantities in terms of the states, $(z(t),\dot{z}(t))$. The general form of the output equation is:

$$z(t) = g(z(t),\dot{z}(t),\ddot{x}(t)). \tag{4}$$

Typical response quantities are absolute acceleration, $\ddot{x}(t)$, relative displacement, $z(t)$, and relative velocity, $\dot{z}(t)$, or functions thereof. The output equation can be a vector equation when more than one response quantity is of interest. In this research, the response quantity of interest is specific energy, or energy per unit mass.

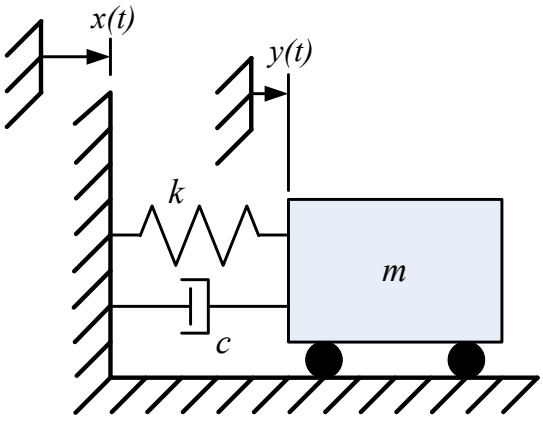


**Figure 3. Single Degree of Freedom Base Excited System**

## 2.1. Energy Response Spectra

The concept of energy spectrum is based on the law of conservation of energy. Conservation of energy requires that all the energy input to a system must be absorbed, dissipated, or converted to kinetic energy. Shock loading transmits energy to a system in a very short time which may then alter or damage the system. The relationship for energy imparted to a system was presented by Zahrah and Hall in their derivation of earthquake energy relations [4].

$$E_I^* = \int_0^z m\ddot{z}(t)dz + \int_0^z c\dot{z}(t)dz + \int_0^z R^* z(t)dz. \tag{5}$$

In Equation (5), $m$ is the system mass, $c$ is the damping coefficient, $z(t)$ is the relative displacement of the system with respect to ground, and $R^*$ is the system restoring force. The input energy $E_I^*$ in the above equation is given in terms of the base or ground acceleration $\ddot{x}$ by the integral:

$$E_I^* = -\int_0^z m\ddot{x}(t)dz = -m\int_0^z \ddot{x}(t)dz. \tag{6}$$

Since the integral relations in Equations (5) and (6) can be calculated independently of the system mass, the equations can be redefined in terms of energy per unit mass. Thus, the expressions become:

$$E_I = \frac{E_I^*}{m} = -\int_0^z \ddot{x}(t)dz \tag{7}$$

$$E_I = \int_0^z \ddot{z}(t)dz + 2\zeta\omega\int_0^z \dot{z}(t)dz + \int_0^z Rz(t)dz. \tag{8}$$

In Equation (8), Zahrah and Hall, replaced the system restoring force term $R^*$ with the mass normalized value $R$ by which they defined $Rz(t)$ to represent the resistance per unit mass of the system or structure, which is equal to $\omega^2 z(t)$. Thus, it is apparent that Zahrah and Hall used the variable $R^*$ to represent the system stiffness which is more commonly denoted $k$ in the mechanical engineering literature and $R = k/m$.

To simplify the numerical integration, the integrals in Equations (7) and (8) are converted to time domain integrals by the relationship $dz = \dot{z}dt$. This is advantageous since the data are traditionally collected as acceleration time histories. Thus, after performing the change of variables, substituting for $R$, and equating Equations (7) and (8), the energy expression becomes:

$$-\int_0^T \ddot{x}(t)\dot{z}(t)dt = \int_0^T \ddot{z}(t)\dot{z}(t)dt + 2\zeta\omega\int_0^T \dot{z}(t)^2 dt + \omega^2\int_0^T z(t)\dot{z}(t)dt. \tag{9}$$

The first term on the right-hand side of Equation (9) represents the kinetic energy, $E_K$, of the system. The second term represents the energy dissipated by damping, $E_D$. The third term represents the sum of the hysteretic energy, $E_H$, plus the strain energy, $E_S$. The previous integral expressions can be shown to be identical to the matrix notation energy balance expressions presented by Edwards [5] and is summarized as:

$$E_I(t) = E_k(t) + E_D(t) + E_A(t). \tag{10}$$

Equation (10) can be viewed as a three-term decomposition of the total energy. It should be noted here that rigid body motion has no specific relative kinetic energy—only oscillatory motion with relative velocity between the base and mass has relative kinetic energy.

The two most common energy spectra metrics currently selected for use in a system margin assessment are the absorbed energy and dissipated energy spectra as defined by the previous equations. However, any of the four energy spectrum terms could be used for a margin assessment if the domain of applicability were well understood. In theory, it is also possible to use any of the above energy metrics as a measure of relative severity between two events.

A response spectrum is a plot of a single degree of freedom oscillator output quantity of interest as a function of the oscillator's natural frequency and damping ratio. The specific energy response spectra are simply the specific energy terms defined previously, evaluated at values of $\zeta$ and $\omega$ corresponding to the sequence of single degree of freedom oscillators, just as in the SRS.

The maximum energy response spectra are the infinity norms of the individual energy terms:

$$\begin{aligned}
E_{KM}(\Omega,\zeta) &= \left\|\bar{E}_K\right\|_\infty = \max_t \left|E_K^R(t,\zeta,\Omega)\right| \;\forall\, \zeta,\Omega;\, 0 \le t \\
E_{D_M}(\Omega,\zeta) &= \left\|\bar{E}_D\right\|_\infty = \max_t \left|E_D(t,\zeta,\Omega)\right| \;\forall\, \zeta,\omega;\, 0 \le t \\
E_{A_M}(\Omega,\zeta) &= \left\|E_A\right\|_\infty = \max_t \left|E_A(t,\zeta,\Omega)\right| \;\forall\, \zeta,\omega;\, 0 \le t \\
E_{I_M}(\Omega,\zeta) &= \left\|E_I\right\|_\infty = \max_t \left|E_I(t,\zeta,\Omega)\right| \;\forall\, \zeta,\omega;\, 0 \le t
\end{aligned} \tag{11}$$

The specific maximum energy spectra satisfy the triangle inequality:

$$E_{K_M} + E_{D_M} + E_{A_M} \ge E_{I_M},\; \forall\, \zeta,\Omega;\, 0 \le t. \tag{12}$$

Two values of $t$ are usually of interest. The first is the duration of the excitation, $T_E$. The energy spectra at $t = T_E$ are the residual energies that cause free vibration of the system. The other time of interest is the time at which the system returns to rest. Just as the oscillator starts at rest, it must eventually return to a vibration-free state if the damping is non-zero. This "return to rest time" can be $t = \infty$, for notational convenience. This assumes a purely linear system, which implies that there is no permanent deformation in the system post-shock. When the linear system returns to rest, $E_A(\infty) = E_K(\infty) = 0$, and from Equation (10), $E_D(\infty) = E_I(\infty) = E_I(T_E)$, since $\ddot{z}(t) = 0$

for $t \geq T_E$. The energy spectra reach steady state once the transient decays to zero since energies are conservative and the duration is finite.

## 2.2. Rotational Shock Response Spectrum

Traditionally the shock response spectra have been applied to translational shocks. Inherent in that assumption is the restriction that the foundation does not rotate. If rotation motions of the foundation develop significant acceleration components, such as with a 6-DOF shaker system, then the assumption of translational inputs is no longer valid and significant errors can be introduced by ignoring these components. A brief development of the rotational shock response spectra theory is presented here as background for development of the 6-DOF test results presented later in this report.

The concept of a rotation spectra follows from the same derivation as for the translational shock spectra [14]. It is assumed that a single degree-of-freedom system is subject to a forced base rotation, $\theta(t)$, with a small angular amplitude such that $\sin\theta \cong \theta$ and centripetal and Coriolis accelerations are negligible. A sketch of the system is shown in Figure 4 and the equation of motion is given as:

$$m\ddot{x} + kx = -m\ddot{\theta}l. \tag{13}$$

Dividing through by the mass gives:

$$\ddot{x} + \omega^2 x = -\ddot{\theta}l. \tag{14}$$

In the above equations $x$ is the relative motion of the oscillator mass, $m$, with respect to the rotating coordinate system and $l$ is the distance from $m$ to the foundation center of rotation. Making the usual assumption that the initial relative displacement and velocity is zero gives a solution of the form:

$$x(t) = \frac{l}{\omega}\int_0^t \ddot{\theta}(\tau)\sin\omega(t-\tau)d\tau. \tag{15}$$

This is identical to the undamped translational case except that $z(t)$ is replaced by $l\theta(t)$. For the case where both translation and rotation occurs, the two motions can typically be considered separately, with two spectrum curves being developed. The responses from the two spectrum curves can then be combined to yield a composite shock response spectrum. The specific method of combining two or more SRS will be discussed in greater detail later in this paper. In single axis testing, the usual method is simply to take the maximum envelope of all the various SRS. However, for multi-axis shocks there does not appear to be an accepted method for combining multiple SRS at this time.

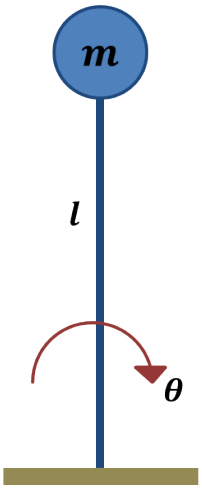


**Figure 4. Rotational Spectra Coordinate System.**

## 2.3. 6-DOF Composite Spectra

Calculating the shock response spectra for a single translation input is a simple task. Extending the shock response spectra to account for rotation is also relatively straightforward although by no means common. The problem encountered here is the need to extend the SRS to account for a full 6-DOF input and compare the resulting SRS with a single degree-of-freedom SRS known to produce failure a failure in the same type of components.

Since it is well known that velocity has a direct relationship with stress [15], the pseudo-velocity SRS will be used to generate a composite 6-DOF SRS. Since failure is related to strain, and hence stress, it is hypothesized that a stress based formulation for generating a composite 6-DOF SRS will yield the best results. Figure 5 shows a hypothetical cantilever beam oriented with respect to the 6-DOF coordinate system. Here, the x-axis is oriented parallel to the cantilever beam's long axis but not necessary collinear with the axis of the beam. This coordinate system corresponds well with the actual 6-DOF shaker coordinate system where it is assumed that the table's center of rotation is at the geometric center of the table face but the part under test will of necessity be mounted some distance above the table face.

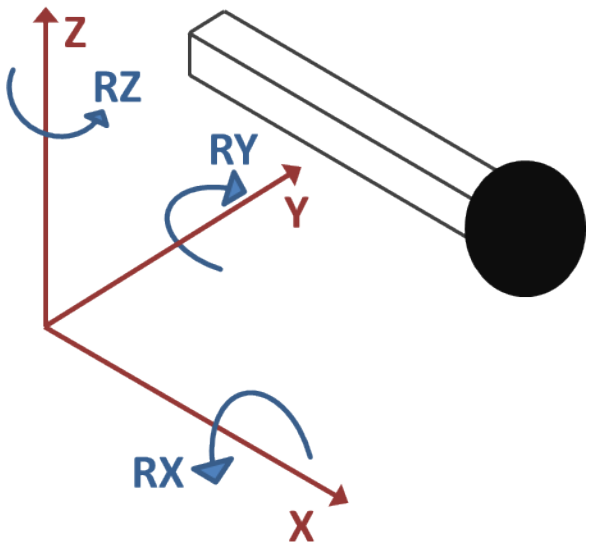


**Figure 5. Cantilever Beam and Coordinate System**

From the coordinate system shown in Figure 5, it is readily apparent that a shock in the y- or z-axes will produce a moment, $M$, about the base of the cantilever beam generating stress given by the familiar equation:

$$\sigma = \frac{Mc}{I}, \tag{16}$$

where $I$ is the beam's area moment of inertia, and $c$ is the distance from the neutral axis to the outer surface. It is also apparent that a rotational shock about the z-axis will produce y-axis bending stress similar to the bending stress from a translational y-direction shock. Likewise, a rotational shock about the y-axis will augment the z-direction translational shock stress. On the other hand, an x-direction shock produces stress that is fundamentally different since the shock here acts along the axis of the beam as an axial force and generating a stress given by the familiar equation:

$$\sigma = \frac{F}{A}. \tag{17}$$

However, in contrast to the above relations, a rotational shock about the x-axis would impose a twist in the beam if the x-axis was collinear with the beam axis or a bending load if the beam is offset from the x-direction center of rotation as shown here. In the case shown here and tested in the laboratory, the beam x-axis was above the table by several inches, thus it is assumed here than a rotational shock about the x-axis produces a y-direction bending stress. To combine the stresses produced by the 6-DOF shaker shock the stress in each of the three axes are given by the relations:

$$\sigma_x = \frac{F}{A}, \tag{18}$$

$$\sigma_y = \frac{F_y lc_y}{I_{zz}} + \frac{T_z lc_y}{I_{zz}} + \frac{T_x hc_y}{I_{zz}},$$

$$\sigma_z = \frac{F_z lc_z}{I_{yy}} + \frac{T_y lc_z}{I_{yy}}.$$

In the above equations, $l$ is the cantilever beam length and thus $Fl$ represents the moment generated from a translational shock and $Tl$ represents the moment generated from the rotational shock about the foundation. The $h$ in Equation (18) represents the height of the cantilever beam above the shaker table. Since there is a direct relationship between the pseudo-velocity and stress, the above relationships can be written in terms of the effective pseudo-velocity SRS (PV) in an axis:

$$\begin{aligned} PV_{xeff} &= PV_x \\ PV_{yeff} &= PV_y + PV_{rz} l + PV_{rx} h \\ PV_{zeff} &= PV_z + PV_{ry} l \end{aligned} \tag{19}$$

To combine the stresses shown in Equation (18) and hence the pseudo-velocity SRS in Equation (19), it is necessary to combine like stress types. Bending stress in the y- and z-directions will combine to a stress vector in the y-z plane. Thus, the total bending stress is the square root sum of the squares of the y- and z-direction bending stresses. Likewise, the effective pseudo-velocity SRS for bending would be the square root sum of the squares of the effective y- and z-direction SRS. The x-direction stress is simply additive to the bending stress; however, simply adding the x-direction SRS to the bending SRS inherently assumes that the shock induced stress is the same in the axial and bending directions for the same shock. This is clearly not the case. Therefore, to combine the x-direction SRS with the bending SRS, it is necessary to scale the x-direction SRS according to its ability to generate stress proportional to the bending stress. It is hypothesized that the x-direction scale factor is the ratio of the axial to bending stress from the same applied load, $F$, and would be given by:

$$\frac{\sigma_A}{\sigma_B} = \frac{F/A}{Mc/I} = \frac{FI}{AMc} = \frac{F\frac{1}{4}\pi r^4}{\pi r^2 Flr} = \frac{r}{4l}. \tag{20}$$

Thus, for the cantilever beam shown in Figure 5, the composite pseudo-velocity SRS from a 6-DOF shock input is assumed to be given by the relationship:

$$PV_{composite} = PV_{xeff}\frac{\sigma_A}{\sigma_B} + \sqrt{(PV_{yeff})^2 + (PV_{zeff})^2}. \tag{21}$$

Likewise, there should be a similar relationship for the energy spectrum. It is well known that the maximum absorbed energy spectrum is related to the pseudo-velocity shock response spectrum by the equation:

$$E_{Am} = \frac{1}{2}PV^2. \tag{22}$$

However, the absorbed energy cannot be combined in quite the same way as the SRS since the absorbed energy spectrum already contains the SRS squared. To make the same relationship work, the energy must be written in terms of the pseudo-velocity as:

$$PV = \sqrt{2E_{Am}}. \tag{23}$$

Substituting the corresponding x-, y-, and z-direction translational and rotational absorbed energy spectra into Equation (19) and then into Equation (21) quickly becomes very tedious to solve analytically as the cross terms multiply. However, the equations are readily solved numerically by simply performing the conversion in Equation (23) and substituting that result back through Equations (19) and (21). While this should work well, it is not particularly satisfying from the standpoint of utilizing energy metrics as a substitute for the more traditional shock spectra. It is also hypothesized that the same scaling methodology should work for input and dissipated energy as well since all three energy types are related as was previously discussed.

The advantage to the methodology presented here is that the full spectrum is retained for all frequencies. An alternative method of combining multi-axis results was presented by Edwards using an equivalent margin based on a normalized energy [16]. The premise being that different axes usually have different energy requirements. This margin method ensures a weighting in the sum. The advantage is that a single scalar value is obtained for comparison, and likewise the disadvantage is the loss of the information contained in the full spectrum. Edwards' method starts with the fact that the total energy is simply the sum of the energies in each axis, thus:

$$E_{Total} = E_x + E_y + E_z. \tag{24}$$

Here again the assumption is for translational inputs only so some adjustment to Equation (24) is necessary to accommodate the rotational shock inputs applied here. However, instead of simply summing the energies in each direction, Edwards proposed summing a normalized energy from each direction. Thereby accounting for the differences in energy requirements to generate failure in a specific axis. To accomplish that, Equation (24) is written as:

$$Margin = \frac{E_x}{E_{x\,fail}} + \frac{E_y}{E_{y\,fail}} + \frac{E_z}{E_{z\,fail}}. \tag{25}$$

From Equation (25), it is clear that if the resulting sum is greater than one then the component should have failed and if the sum is less than one the component should have survived. Adding the rotational energies into Equation (25) has not been previously addressed. The energy terms developed here are actually expressed as an energy per unit mass as opposed to a true energy. However, rotational energies are calculated in terms of energy per unit rotational moment of inertia. Thus, the units of rotational energy contain an extra length squared term. The energy units for both translational and rotation energies are given in Table 1.

**Table 1. Translational and Rotational Energy Spectrum Units**

| Translational Energy Units | Rotational Energy Units |
|---|---|
| $\frac{ft - lbf}{slug}$ | $\frac{ft - lbf}{slug\ ft^2}$ |

To incorporate the rotational energy terms, the same philosophy proposed for combining the pseudo-velocity SRS above is again used. The rotational shock applies a loading analogous to the translational shock when applied through the center of mass. Thus, the rotational pseudo-velocity spectrum was multiplied by the effective length, here the rotational energy should likewise be multiplied by the effective length squared making the units consistent.

This is fundamentally different than the composite pseudo-velocity SRS method described above which was derived based on combinations of stress in three directions. In addition, there is no concept of an energy spectrum at failure. Rather, the failure energy is the energy at the system's fundamental modes or perhaps the modes related to a known failure. Thus, the failure energies in Equation (25) are the failure energies at a specific frequency and axis. For a simple system like a cantilever beam, the failure is related to the lowest few bending modes and is relatively straightforward to calculate. For a very complicated system this could become quite complex.

# 3. FATIGUE THEORY

Endurance of materials subject to cyclic loading has been extensively studied since the 1800's. The endurance life or fatigue life, defined as the number of cycles to failure or the ability of a machine part to resist fatigue, is dependent on the developed stress in the part. The data from these tests characterizing the endurance of the material are displayed as S-N curves. The S-N curve in the high-cycle fatigue region can be represented analytically. The most popular representation is the Basquin relation:

$$NS^b = C. \tag{26}$$

In the above equation, $N$ is the number of cycles to failure, $S$ is the cyclical stress amplitude, $b$ is the fatigue strength coefficient, and $C$ is an empirically determined constant. The fatigue strength coefficient is determined from S-N data where $-1/b$ is the slope of the S-N line in log-log space.

Basquin's equation is a model based on test data. Fatigue strength coefficients typically range from 3 – 25 with the most common values falling between 3 and 10. Lalanne [17] has compiled typical fatigue strength coefficient values for a variety of materials (aluminum, steel, solder) and components (resistors, capacitors, circuit boards, and other complex electronic items) measured from numerous tests. The spacecraft community has settled on a fatigue strength coefficient of 4.0 for electronic and electrical equipment, 6.4 for load carrying structures under sinusoidal vibration, and 8.0 for load carrying structures under random vibration [18, 19].

Basquin's equation is popular and has been used for more than 60 years for several reasons: it fits measured data well; it is consistent with fracture mechanics models; and it can be adjusted to account for factors such as surface finish, corrosion, stress concentration factors, stress ratios, and others as needed.

It is postulated that a power law relationship like Basquin's equation applies to shock environments and energy spectra comparisons. In this context, the Basquin equation would be defined in terms of some energy quantity and number of cycles to failures.

## 3.1 Input Energy and Fatigue Life

In the energy framework, fatigue life is a function of the input energy, which can be calculated for any dynamic system as:

$$E_I = \int_{t=0}^{t=T} p(t) \cdot \dot{x}(t) dt \tag{27}$$

where $p(t)$ is an external load vector and $\dot{x}(t)$ is the response velocity vector. Note that input energy includes a response term. This means that the input energy can vary across a structure depending on the response location. In the subsequent development, there is an implicit assumption that the input energy is calculated for the component of interest.

The S-N plot is the experimentally determined relationship between zero mean, constant cyclic stress amplitude and number of cycles to failure. To create a similar $E_I$-N curve from an S-N curve, consider the case of constant amplitude cyclic loading. In this case $p(t) = A\sin(\Omega t)$, and any environment is characterized by $[p(t),T]$ or $[A,\Omega,T]$. For steady state cyclic loading, the input energy can be written as:

$$E_I = \int_{t=0}^{N/\Omega} p(t)\dot{x}(t)dt = N\int_{t=0}^{1/\Omega} p(t)\dot{x}(t)dt = N\overline{E_I} \tag{28}$$

where $N$ is the number of cycles and $\overline{E_I}$ is the input energy per cycle.

Input energy per cycle has another interpretation—as the energy dissipated per cycle. If a dissipative system starts and ends at rest, with no permanent deformation, the total input energy is equal to the total dissipated energy, $E_I = E_D$. So, it follows by extension that $\overline{E}_I = \overline{E}_D$.

This relationship can be used to generate the $E_I$-N curve. Damping energy is proportional to the square of the stress amplitude, $S$, in linear dynamical systems with viscous damping [20]. Thus, it is apparent that

$$\overline{E}_D \propto S^2 \tag{29}$$

Substituting Equation (29) into Equation (26) implies that dissipated energy also follows a power law relationship with the number of cycles.

$$N\overline{E}_D^{\frac{b}{2}} = C_D \tag{30}$$

where $C_D$ is an empirically determined constant, not necessarily the same as $C$ from Equation (26). Rearranging this equation gives:

$$\overline{E}_I = \overline{E}_D = C_D^{\frac{2}{b}} N^{-\frac{2}{b}} \tag{31}$$

This form of the equation is consistent with the way S-N curves are shown graphically whereas the original form of Equation (26) is consistent with fracture mechanics models. The slope of the S-N curve is $-1/b$, so the slope of a corresponding $\bar{E}_I$-N curve is twice the slope of the S-N curve. Thus, in terms of total input energy or total dissipated energy, Equation (31) becomes

$$E_I = E_D = N\overline{E}_I = C_D^{\frac{2}{b}} N^{\left(1-\frac{2}{b}\right)} \tag{32}$$

While damping energy is approximately proportional to the square of stress amplitude as shown in Equation (29), Dowling provides a more realistic relationship between stress and damping energy as a non-linear function of stress amplitude [20]. For metals, this relationship is given as

$$\overline{E}_D \propto S^{\beta} \begin{cases} \beta \sim 2.4, S < 0.8S_{yield} \\ \beta \sim 8\ , S \geq 0.8S_{yield} \end{cases} \tag{33}$$

Thus, the more general form of Equation (33) is:

$$\bar{E}_I = C_D^{\frac{\beta}{b}} N^{-\frac{\beta}{b}} \tag{34}$$

For high-cycle fatigue, generally, $S < 0.8 S_{yield}$ suggesting that $\beta = 2.4$ is appropriate and slightly more conservative than $\beta = 2$. A common average value for the fatigue strength coefficient for general structural members is $b = 6.67$ which is consistent with References 18 and 19. The slope of the S-N curve is then $-1/b \cong -0.15$, so a typical slope of the $\bar{E}_I$-N curve is about −0.36 and the slope of the corresponding $E_I$-N curve would be 0.64.

The main implication of the similarity between the S-N curve and the $\bar{E}_I$-N curve is that all of the machinery developed for high-cycle fatigue analysis is applicable when the quantity of interest is input energy instead of stress—specifically Miner's rule.

## 3.2. Cantilever Beam Dissipated Energy Example

A cantilever beam example can be used to illustrate the relationship of dissipated energy to steady-state cyclic loading. Figure 6 shows a sketch of this simple system consisting of a base excited cantilever beam of length $l$, with a tip mass, $m$. If a steady-state excitation is applied at the clamped end, the beam will translate and deform as the inertia force of the mass resists the beam's movement.

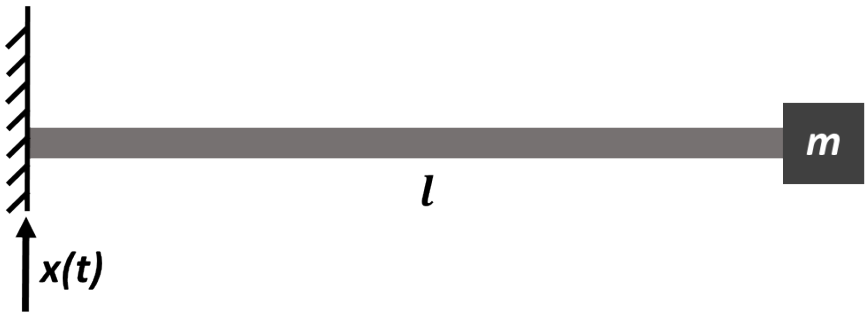


**Figure 6. Cantilever Beam with Tip-Mass and Base Excitation**

The cantilever beam in Figure 6 can be equally well represented by a variable force at the beam tip as shown in Figure 7. In Figure 7, the tip force is designed to make the stress in the beam equivalent to the stress experienced by the configuration shown in Figure 6 without loss of generality.

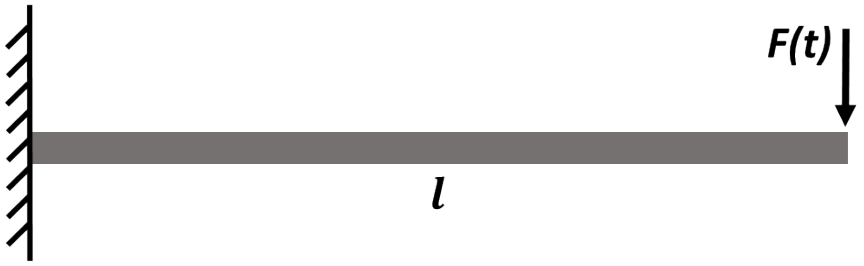


**Figure 7. Cantilever Beam with Tip Force Loading**

The work done by the force is given by:

$$W = \int_{x_i}^{x_f} F(x)dx. \tag{35}$$

Since the cantilever beam is essentially a spring, the work done in displacing a spring is given by

$$W = \frac{1}{2}kx^2. \tag{36}$$

For the cantilever beam, the stiffness, $k$, is equal to

$$k = \frac{3EI}{l^3} \tag{37}$$

where $E$ is the modulus of elasticity, $I$ is the area moment of inertia, and $l$ is the length. The maximum deflection is at the free end and the maximum bending moment and maximum stress all occur at the clamped end. The deflection, as a function of time, is given by:

$$y(t) = \frac{l^3}{3EI}F(t). \tag{38}$$

Likewise, the maximum bending moment is

$$M(t) = lF(t). \tag{39}$$

Finally, the stress as a function of the applied force is:

$$\sigma(t) = \frac{cM(t)}{I} = \frac{cl}{I}F(t) \tag{40}$$

where $c$ is distance from the neutral axis to the outer surface of the beam—half the thickness of the beam in this case.

For simplicity, assume that the forcing function can be represented by the function:

$$F(t) = A\sin(\omega t). \tag{41}$$

Substituting the assumed force into Equation (40), the stress as a function of time is given as

$$\sigma(t) = \frac{cl}{I} A \sin(\omega t). \tag{42}$$

In terms of energy quantities, the dissipated energy is the quantity of interest for vibration problems. From the derivation of the energy relationships shown previously, the dissipated energy is extracted from Equation. (9) as:

$$E_D(t) = 2\zeta\omega \int_0^T \dot{z}(t)^2 dt. \tag{43}$$

In this example, the base has no motion and the displacement at the beam tip represents the SDOF mass motion. Therefore, in this derivation $z(t) = y(t)$. Substituting Equation (41) into Equation (38), taking the time derivative and substituting that into Equation (43) gives:

$$E_D(t) = 2\zeta\omega \int \left[\frac{l^3}{3EI}\omega A \cos(\omega t)\right]^2 dt. \tag{44}$$

Performing the integration yields

$$E_D(t) = 2\zeta\omega \left[\frac{l^3}{3EI}\omega A\right]^2 \left[\frac{1}{2}\omega t + \frac{1}{4}\sin(2\omega t)\right]. \tag{45}$$

To simplify the equations, we define a constant

$$R = \left[\frac{l^3}{3EI}\omega A\right]^2. \tag{46}$$

Note that $R \propto A^2$ as expected. Then

$$E_D(t) = \zeta\omega^2 R t + \frac{1}{2}\zeta\omega R \sin(2\omega t). \tag{47}$$

Equation (47) shows that the dissipated energy has an oscillating component and a linear component. In this example, the stress oscillates about zero because the force oscillates about zero; however, the dissipated energy only increases. This is shown graphically in Figure 8 for one and five loading cycles.

Figure 8 shows that while the force oscillates the dissipated energy in monotonically increasing with each cycle. From *S-N* data, fatigue failures are logarithmic with respect the number of cycles but dissipated energy is linearly increasing with number of cycles. Therefore, dissipated energy as defined above cannot by itself be a reasonable predictor of damage since it does not follow the logarithmic form of the *S-N* data.

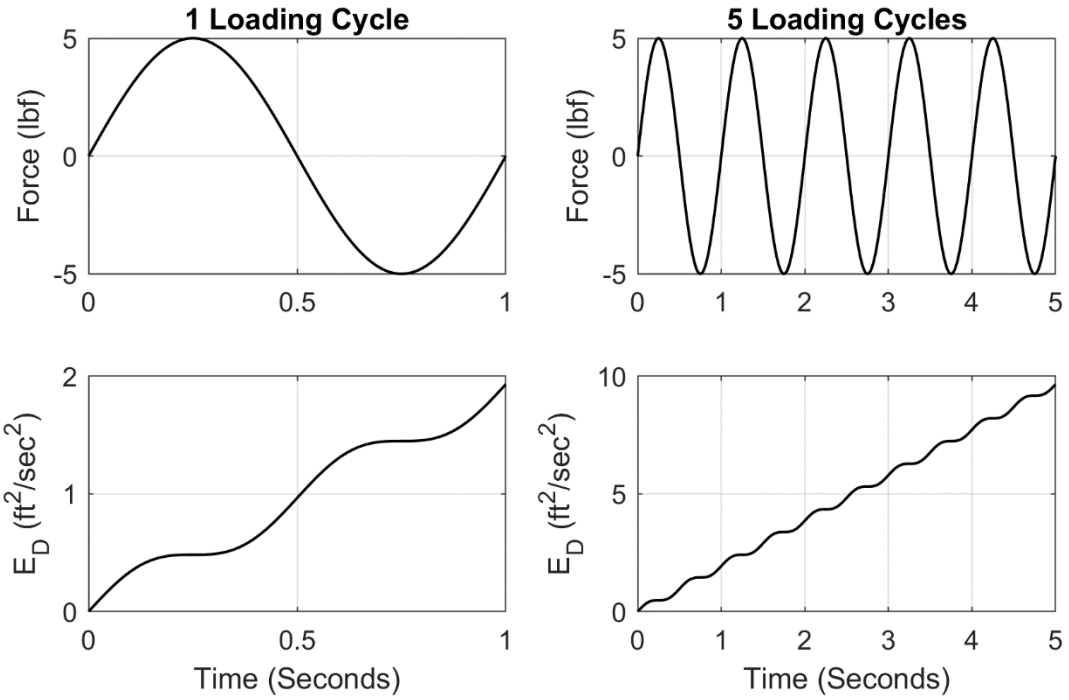


**Figure 8. Force and Dissipated Energy for One and Five Loading Cycles of the Cantilever Beam**

# 4. ENERGY SPECTRUM CALCULATIONS

Calculation of the energy spectrum is relatively straightforward using the previously developed integral relationships although it can become quite time consuming. Typically, the data collected are sampled at a high rate, the records can be long, and several integrations are required to get to the final energy spectrum results. It would be extremely useful to derive a methodology based on single degree of freedom filters like the ISO standard for calculating shock response spectra.

The input energy spectrum, kinetic energy spectrum, and dissipated energy spectrum are all derived from the relative velocity between the base input and the motion of the single-degree-of-freedom oscillator mass. Since the ISO standard includes ramp invariant filter weights for calculating the relative velocity (RV) SRS from measured acceleration data [21], it should be possible to eliminate several integration operations using SRS techniques. Furthermore, it has been previously shown that the absorbed energy spectrum is a function of the pseudo-velocity shock response spectrum [1].

The four previously defined energy spectrum terms can be calculated using the ISO SRS filter weights, fewer integrations, and combinations of two velocity shock response spectra. The input and dissipated energy spectrum still require an integration to be performed although the relative velocity at a given frequency can be more quickly calculated using ramp invariant filters. Thus, the input energy can be calculated by:

$$E_I = -\int_0^T \ddot{y}\, RV\, dt. \tag{48}$$

The dissipated energy is likewise calculated as:

$$E_D = \frac{1}{2}\zeta\omega_n \int_0^T RV^2 dt. \tag{49}$$

The absorbed energy spectrum can be calculated by a straightforward manipulation of the pseudo-velocity SRS as shown.

$$E_A = \frac{1}{2} PVSRS^2. \tag{50}$$

Likewise, the kinetic energy spectrum is a similarly straightforward manipulation of the relative velocity SRS.

$$E_K = \frac{1}{2} RVSRS^2. \tag{51}$$

The above expressions for the energy metrics are considerably faster than the previously defined integral methods. Numerical integration can be quite slow if data records are long and sample rates are high. The ramp invariant filter approach reduced the number of integration steps by half, resulting in a halving of the total computation time.

# 5. TEST ARTICLE DESIGN AND EVALUATION

The bulk of the experimental work for this WSEAT project was performed using 3-D printed ABS plastic cantilever beams made by the Sandia National Laboratories Additive Manufacturing group. These beams were easily made, relatively inexpensive, and features could be easily incorporated into to the test articles. The basic requirements for the test articles are given in Table 2.

**Table 2. Test Article Primary Design Requirements**

| |
|---|
| • Easy and economical to manufacture<br>• Includes a stress concentration zone to control failure mode and location<br>• Tailorable fundamental natural frequency<br>• Tailorable failure load |

Given the uncertainties with 3-D printing plastic components and using the test results for theoretical developments, a significant effort was put forth to characterize the material properties and repeatability of the 3-D printed ABS plastic.

Testing was performed on a drop table in the SNL/NM Mechanical Shock Laboratory, on the SNL/NM large 6-DOF shaker at the Tech Area III vibration facility, and on a small modal shaker in the SNL/NM Component Dynamics Laboratory. Different test specimens were used at different points in this research project depending on the goals of the particular test series. Descriptions of the different cantilever beam styles used for the various tests are presented here.

## 5.1. Elastic Properties of 3-D Printed Beams

To make reasonable predictions of test failures, it is necessary to understand the material properties of the items being tested. A series of static pull tests was performed in the Sandia National Laboratories Structural Mechanics Laboratory (Org. 1528) on various 3-D printed tensile coupons prior to having the full lot of test specimen printed. Cylindrical specimens, modeled after the ASTM D638 rigid rod specimen, were used; however, modifications were required to accommodate the grip in the tensile test machine. Tensile coupons were manufactured using a 5 mil and 10 mil print head and lengthwise (coupon printed horizontally on the bed) and crosswise (coupon printed vertically on the bed) raster directions. During this phase of the study, it was discovered that the 3-D printer had several properties that significantly affected the strength and performance of the resulting beams. The results from the various tensile tests are presented in Figure 9. The inset photograph in Figure 9 shows a micrograph of the fracture surface from one of the crosswise raster tensile specimen. The failure occurred between print layers and the raster pattern is readily discernable.

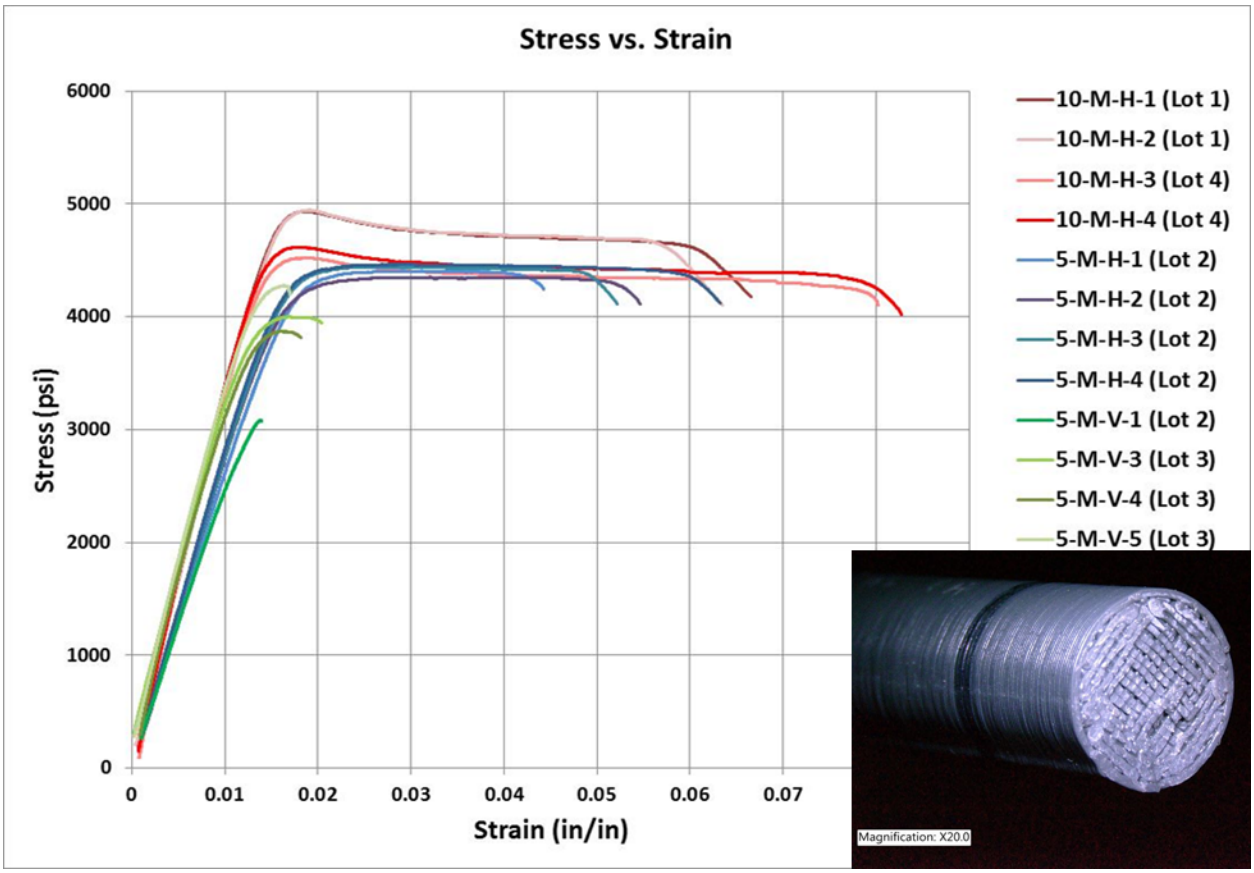


**Figure 9. Stress-Strain Data from Tensile Specimen and Inset Picture Showing Fracture Surface for Specimen with Crosswise Raster**

The results indicated that tensile coupons printed in the vertical orientation using a crosswise raster exhibited a brittle failure whereas the coupons printed horizontally on the print bed using a lengthwise raster exhibited a ductile type of failure. The vertically printed specimen also showed more variability in the failure strain than the horizontally printed specimen. It was also noted that the 5 mil print head seemed to have slightly lower strain to failure than the 10 mil print head. A summary of the mechanical properties derived from the tensile testing is given in Table 3.

**Table 3 Properties of 3-D Printed Specimens**

| Specimen Type | Average Modulus (psi) | COV (%) | Average Yield Stress (psi) | COV (%) | Average Peak Stress (psi) | COV (%) | Tensile Elongation at Failure (%) | COV (%) |
|---|---|---|---|---|---|---|---|---|
| 10-M-H | 339750 | 1.9 | 4643 | 4.8 | 4754 | 4.6 | 7.3 | 13.4 |
| 5-M-H | 275400 | 2.6 | 4181 | 1.9 | 4416 | 1.1 | 5.4 | 14.7 |
| 5-M-V | 293840 | 8.9 | 3781 | 13.3 | 3807 | 13.5 | 2.0 | 14.5 |

Almost all the cantilever beams used for the shock tests were manufactured using a 5 mil print head with a crosswise raster. This was intentionally done to produce clear pass-fail results in the cantilever beams tested since brittle failures are typically sudden and total. A few lengthwise raster beams were tested near the end of the project for completeness.

## 5.2. Cantilever Beams for Drop Table Testing

The first set of experiments conducted as part of this WSEAT project were performed on a drop table. For these experiments, three types of cantilever beams were manufactured in two different lengths. The beams were nominally 3 in and 5 in long with a 0.25 in outside diameter. Stress concentration notches were manufactured into the beams near the base that were 0.025 in and 0.050 in deep. Some beams were also made without a stress concentration notch. A photograph of a sample set of these beams is shown in Figure 10.

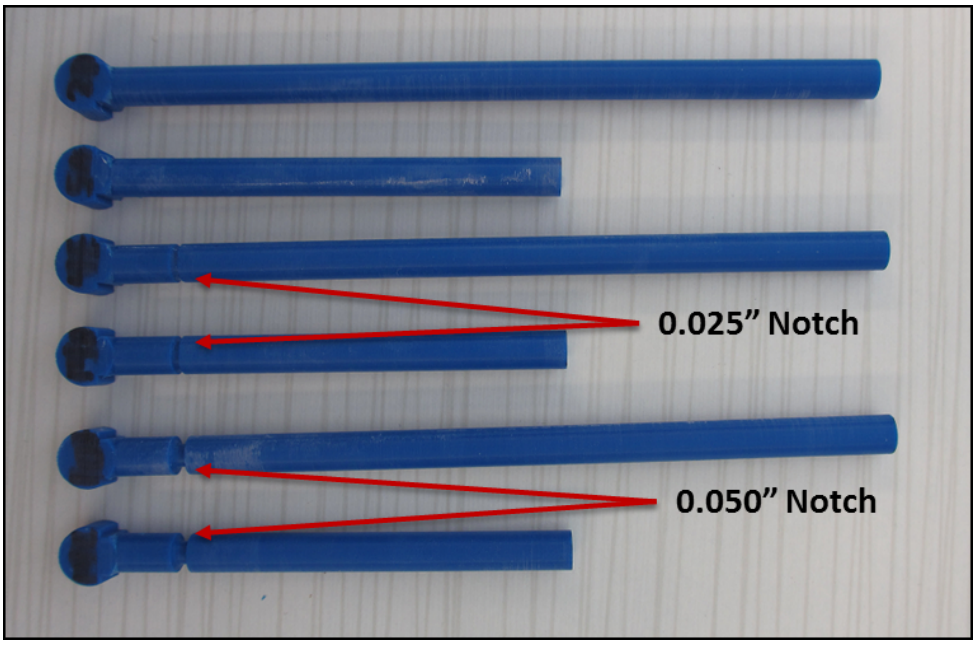


**Figure 10. Photograph of Sample Cantilever Beams Used for Initial Drop Table Testing**

## 5.3. Cantilever Beams for 6-DOF Shaker Testing

Testing on the 6-DOF shaker used both round cantilever beams and elliptic cross-section cantilever beams. The round beams were the same style and properties as those tested previously on the drop table and were used to relate 6-DOF results to prior SDOF results. The elliptic cross-section beams were designed and made specifically for testing on the 6-DOF shaker. The goal being to produce a more complex, multi-axis response. The elliptic cross-section results in a different stiffness in the vertical and lateral directions. In this case, the eccentricity of the beams was relatively small, having a 0.250-inch major diameter and a 0.188-inch minor diameter. The result of using elliptic cross-section beams and 6-DOF shock inputs is that the cantilever beams did not vibrate strictly in a single plane but rather the free end exhibited a more complex motion.

Figure 11 shows a photograph of four elliptical cross-section cantilever beams installed on the 6-DOF shaker table for testing. Figure 11 also shows a micrograph of one of the broken beams detailing the elliptical cross-section as well as the cross-wise raster apparent in the 3-D printing.

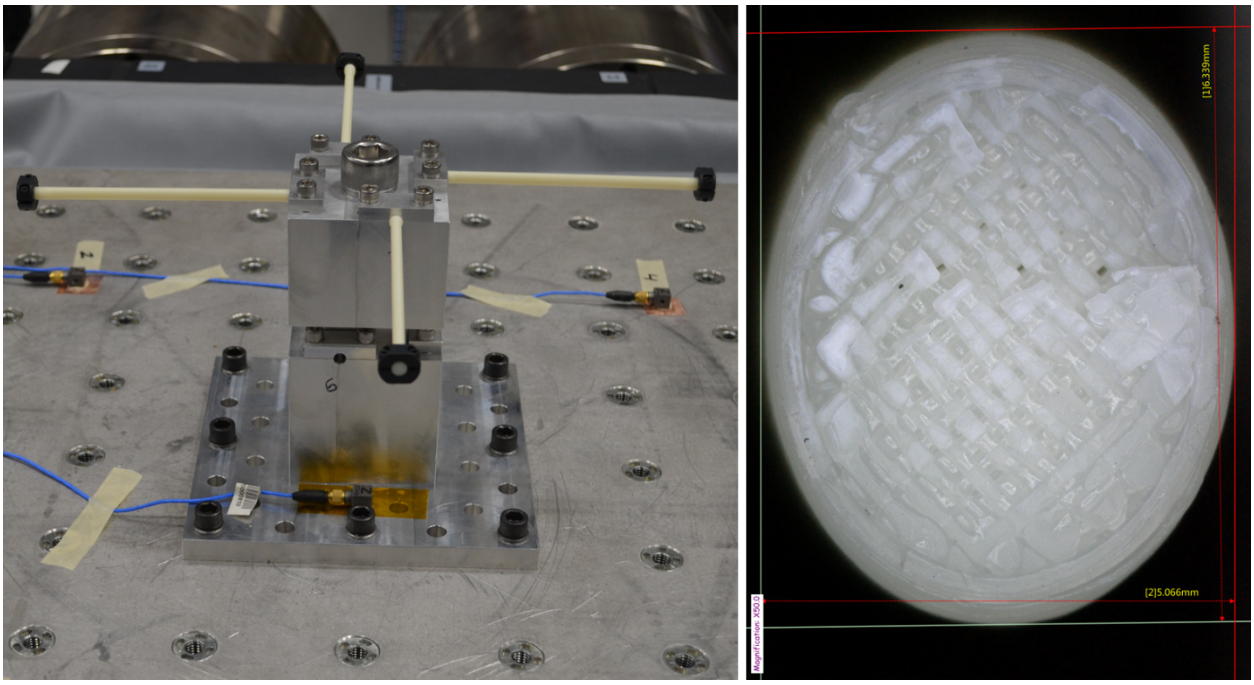


**Figure 11. Photograph of the Elliptic Cross-Section Beams on the 6-DOF Shaker Along with a Micrograph of a Broken Beam Showing the Cross Section and Raster**

## 5.4. Cantilever Beams for SDOF Shaker Testing

The cantilever beams used for the SDOF shaker shock testing were like the original set of round beams used for drop-table testing. Only the five-inch beams with the 0.025-inch notch size were used for this round of testing; however, beams with both cross-wise and length-wise print raster were used. As was previously discussed, the cross-wise raster results in a brittle failure whereas the length-wise raster creates a more ductile failure.

## 5.5. Plate and Simulated Components

In addition to testing cantilever beams, a plate structure with various appendages was designed and manufactured from ABS plastic by 3-D printing. The goal of this test article was to introduce a system with spatial dependence to the study. The purpose being to understand the distribution of failure energy through a more modally rich structure.

All the various appendages were designed with stress concentration notches and locations to accept the same steel or aluminum collars used for weights in the cantilever beam testing. A photograph of the first 3-D printed plate test structure is shown in Figure 12. The 3-D printed

plates were tested both on the modal shaker in the SNL/NM Component Dynamics Laboratory (CDL) as well the drop table in the Mechanical Shock Laboratory. A photograph of one of the plates on the drop table for testing is shown in Figure 13.

The plate was designed with different thicknesses on the right and left half so that different modal responses could be expected for each half, creating a more complex response. The components were designed with between one and three stress concentration zones to encourage failure at various but predictable locations. The components were also designed to use the same steel or aluminum clamp-on collar weights used for the cantilever beam testing.

All the component locations were reconfigurable on the plate, both orientation and position. The components were attached to the plate with small screws adhered into the component base and using nuts on the underside of the plate. Grooves on the bottom of the components interfaced with small ridges on the plate to prevent the components from rotating. As such, the components could only be installed at 90-degree angles to one another.

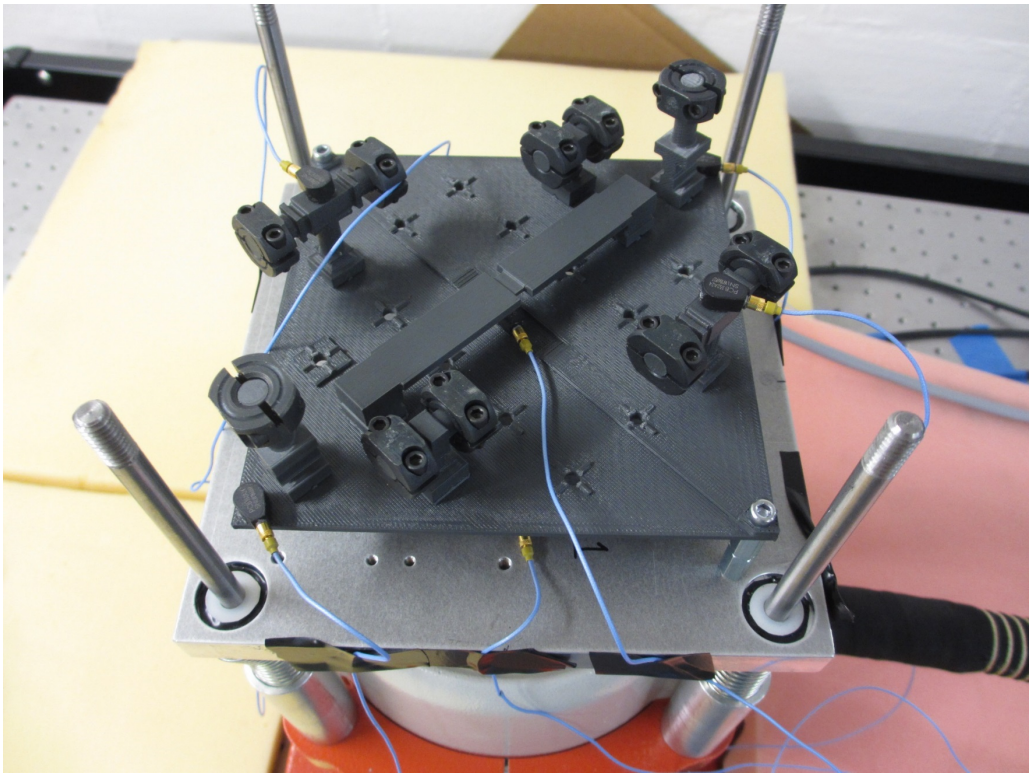

**Figure 12. Photograph of First 3-D Printed Plate Test Structure**

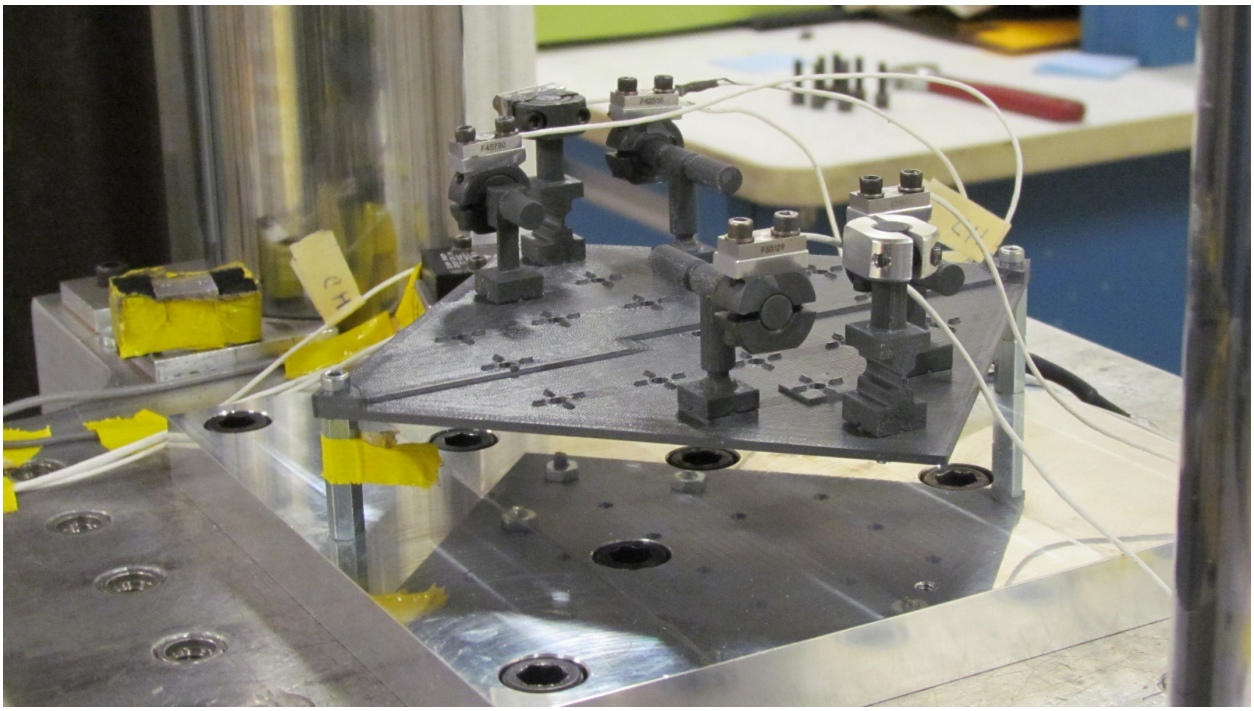

**Figure 13. Photograph of 3-D Printed Plate on the Drop-Table for Testing**

# 6. TEST FIXTURE DESIGN

A test fixture to which impulsive shocks from a drop table, single axis shaker, or 6-DOF shaker could be applied was designed and fabricated. The test fixture is shown in Figure 14. It consists of a base structure that can hold up to eight cantilever beams, which are the shock sensitive components of interest. The primary design requirements are shown in Table 4. A finite element modal analysis showed that the first mode of the base structure is above 1.5 kHz, which is well beyond the excitation bandwidth of interest. The capability to shock eight beams simultaneously provides information on the statistical scatter due to test variability as well as component variability.

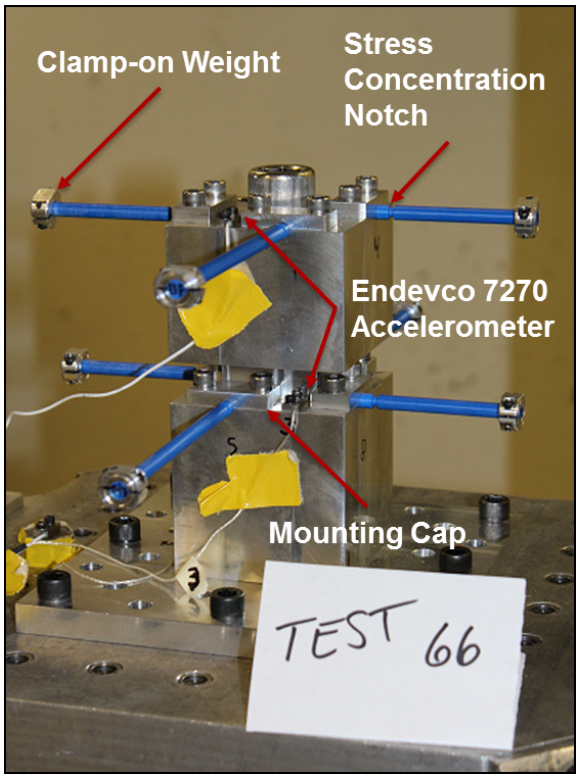


**Figure 14. Photograph of the Test Fixture with 3-D Printed Cantilever Beams Installed**

**Table 4. Test Fixture Primary Design Requirements**

| |
|---|
| • Test multiple test articles simultaneously<br>• Control the test article failure location<br>• Do not unduly influence the dynamic response of the test articles |

The test fixture shown in Figure 14 was intentionally designed with a top and bottom half to support testing of few numbers of beams if desired. This feature was utilized extensively for testing in the Component Dynamics Laboratory (CDL) since the shaker was significantly

smaller. Testing without the top half of the fixture allowed for higher acceleration levels to be achieved. A photograph of this configuration is shown in Figure 15.

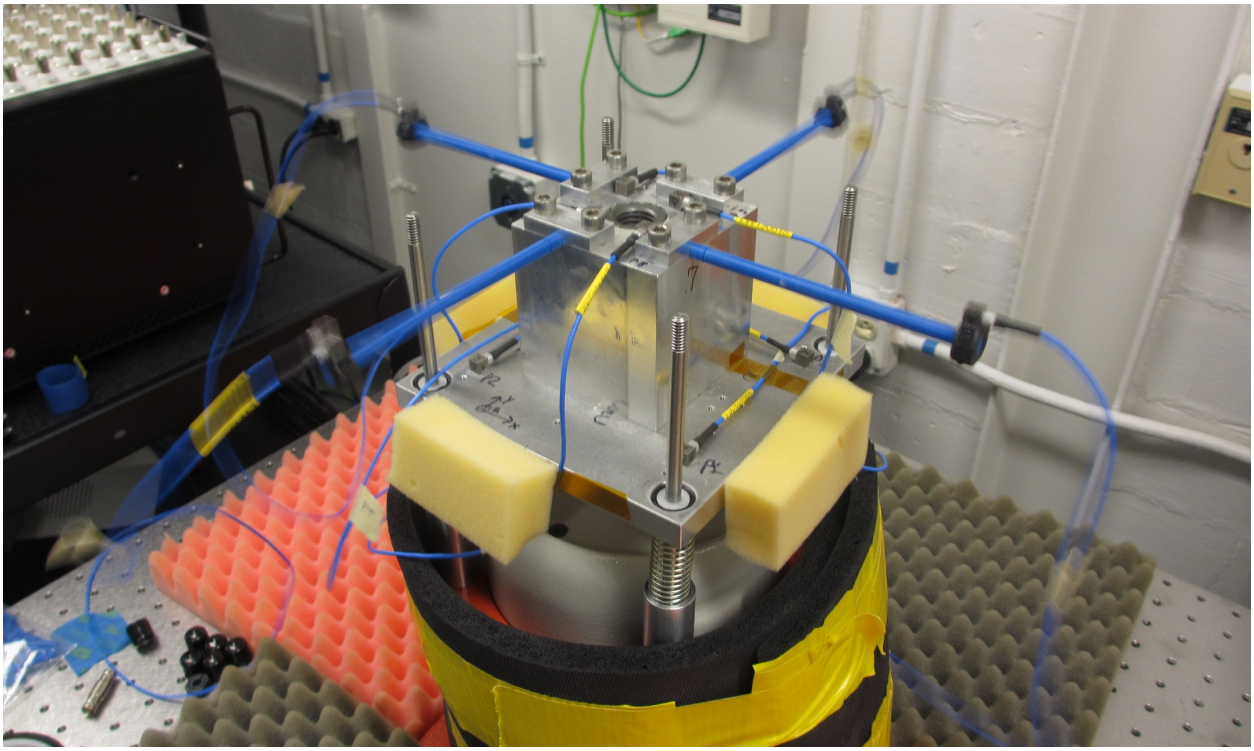

**Figure 15. Photograph of the Test Fixture Used in the Four Beam Configuration**

To allow the CDL modal shaker to push higher accelerations, it was necessary to design a gravity off-load structure to support the weight of the test fixture independently from the shaker armature. A photograph of this structure as-designed and built is shown in Figure 16. This configuration attached the test fixture to the shaker armature directly and supported the weight of the fixture on four soft springs supported by stand-offs from a manufacturer supplied support ring on the shaker. The springs had a natural frequency of less than 3 Hz and had support rods passing through the center of the springs and through holes in the fixture plate to ensure the system alignment. The fixture plate used nylon bushings between the fixture plate alignment holes and the guide rods to eliminate vibration noise from the guide rods impacting the fixture plate.

Before using this design for testing of actual components, a characterization study was completed to ensure that the gravity off-load system was not unduly influencing the response of the articles under test.

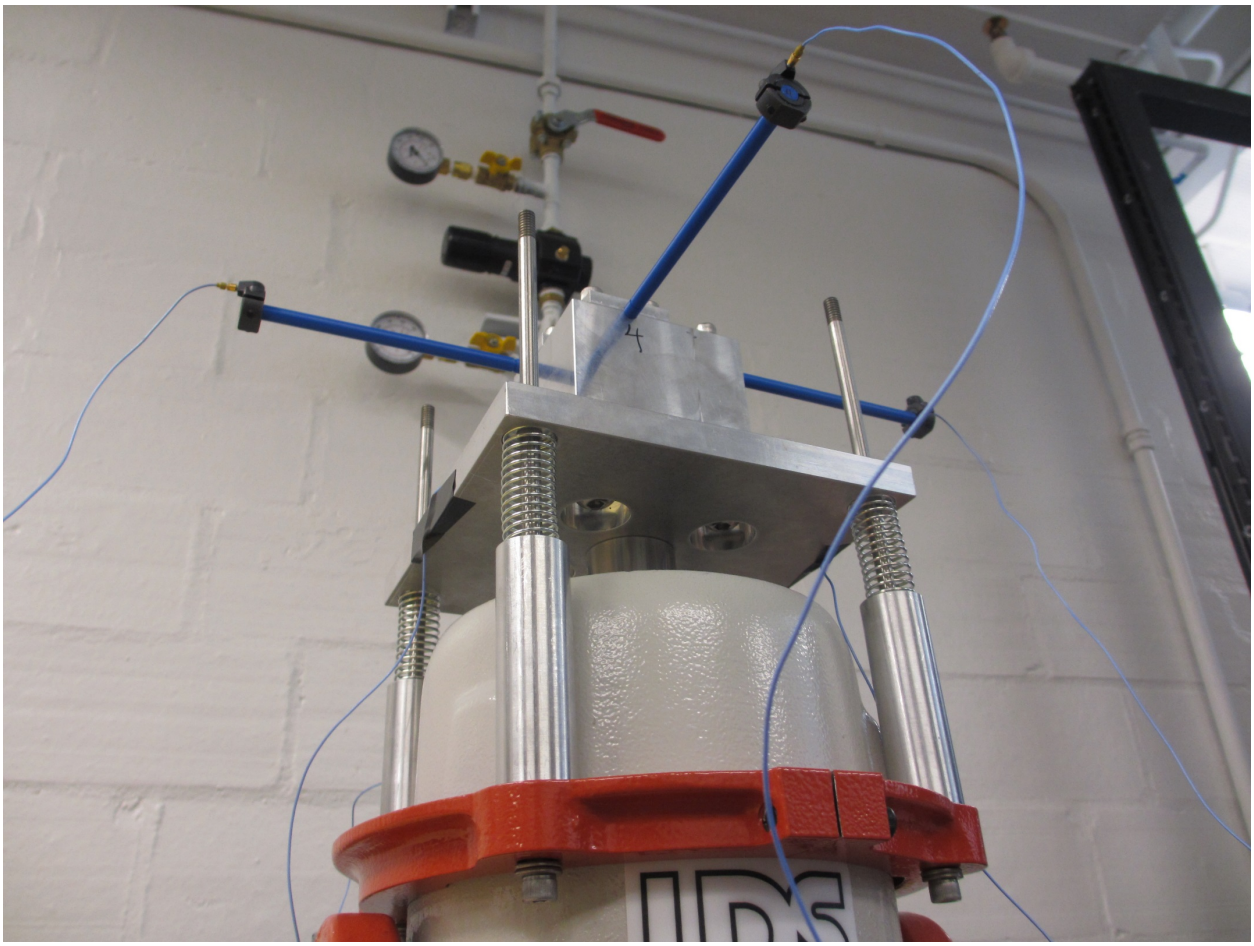

**Figure 16. Text Fixture Attached to Modal Shaker with Gravity Off-Load System**

# 7. CANTILEVER BEAM DROP TABLE TEST RESULTS

The first series of tests for this WSEAT project were performed in the SNL/NM shock laboratory on a drop table in September 2015. For this test series, a total of 72 3D printed cantilever beams were tested on a drop table. The tests were conducted using nine sets of eight beams per test (four 5 inch beams and four 3 inch beams per test) on a drop table. Initial tests were performed by incrementally stepping up the input shock load until all eight beams failed. Typically, most beams failed after just a few shock events. The second round of testing attempted to quantify low-cycle fatigue failures for cantilever beams of the same design. For the low-cycle fatigue tests, a test level less than the failure level was selected and that test was repeated until all beams failed. Figure 17 shows a time history plot from the four accelerometers mounted on the carriage and test fixture during test 70. This profile was typical of the acceleration results seen throughout the testing. Figure 18 shows the acceleration SRS for the carriage mounted accelerometer from the same test, Test 70.

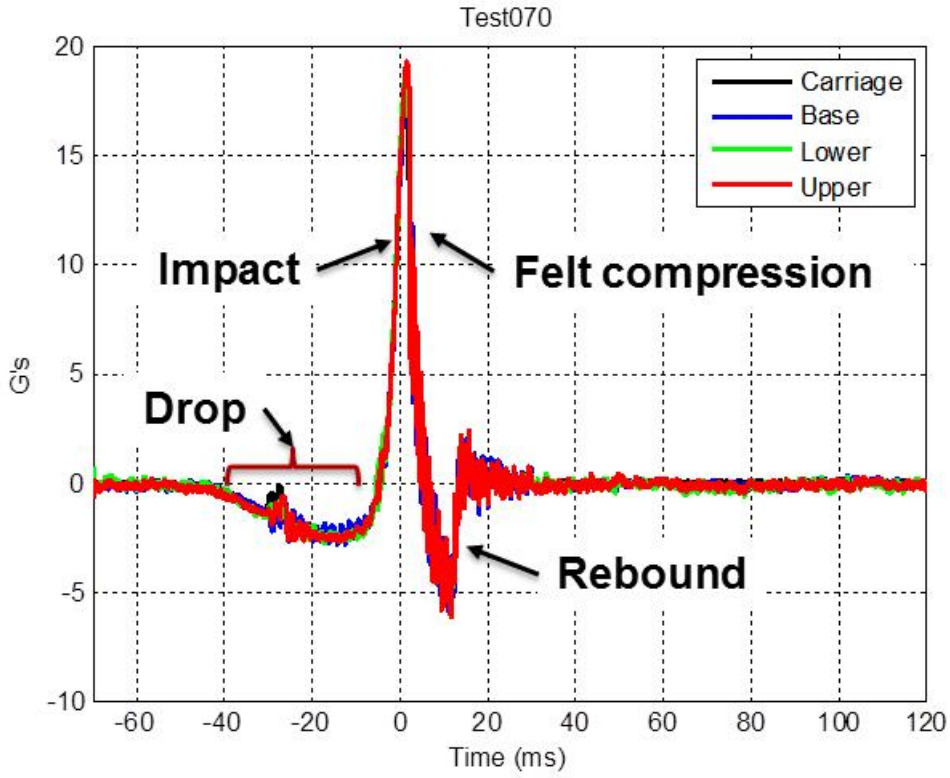


**Figure 17. Typical Acceleration Profile from Drop Table Tests**

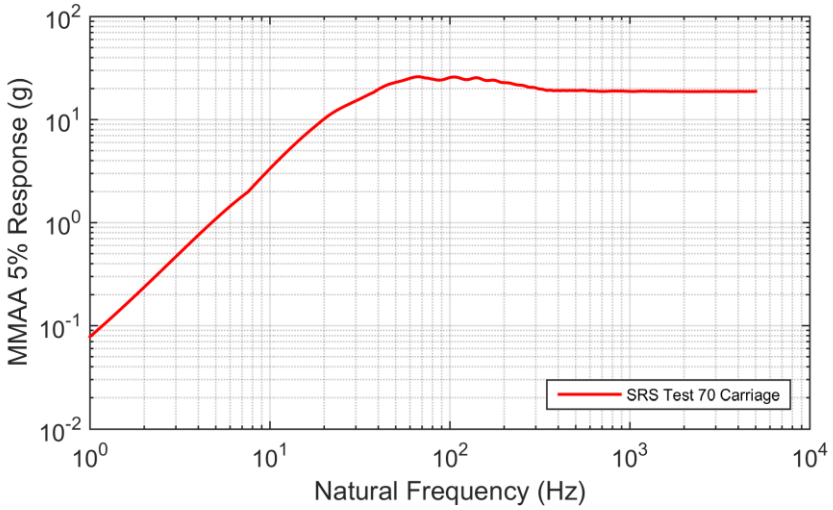


**Figure 18. Typical Acceleration SRS Profile at the Drop Table Carriage**

Approximately 148 shock tests were performed on the drop table. Of these tests, all failures were brittle failures as expected, although some of the beams did not fail completely in a single shock. Some beams cracked and sagged and detached on the subsequent shock. For these beams, failure was considered to have occurred on the first shock that resulted in a visible crack and deformation. Figure 19 shows an interesting photograph taken after Test 70 which shows all three types of failures seen during testing. The beam in the front lower clamp is completely broken free and bounced clear of the table. The beam on the lower right side of the upright is clearly cracked and sagging. The beam on the lower left is severely cracked and apparently hanging by a "thread" of plastic.

The first tests were conducted to determine the failure points of all beam configurations and to compare the finite element beam model predictions to the actual results. Since drop table testing is a series of distinct events with definite increments to the shock load, it is not possible to determine the exact failure point. The cantilever beam specimen would be intact after one shock and fail during the next shock. The exact failure point is then known to be between the last two shocks, but since the tests were conducted incrementally, and the beams were broken, no further refinement was possible. All the drop tests in this portion of the experiments were designed to achieve a nominal 90 Hz haversine pulse. This frequency was selected to ensure that all the beams tested had natural frequencies well below the primary shock pulse frequency. One problem encountered during testing was that the drop table had a minimum shock level. The table available for testing was unable to impart less than about 20g peak acceleration.

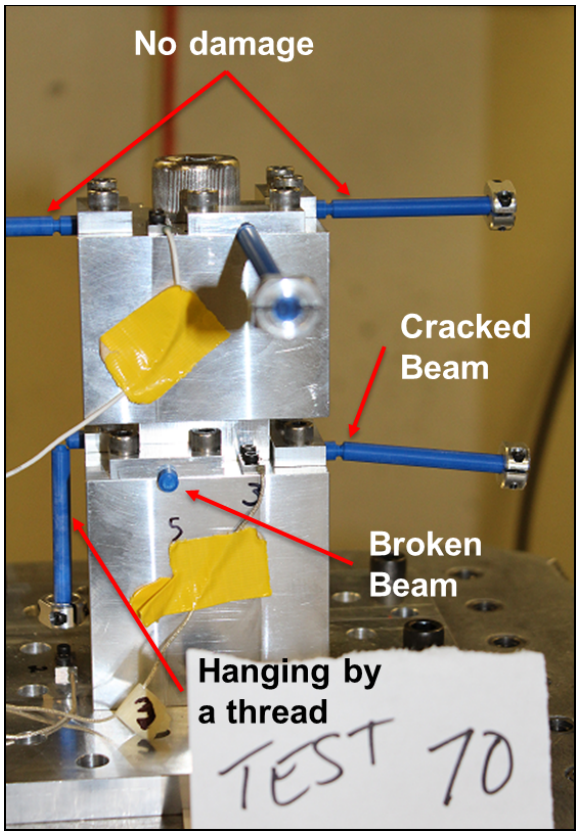


**Figure 19. Summary of Typical Cantilever Beam Failures Types Seen During Shock Testing**

Table 5 summarizes the results from the first passage shock tests. For this test series, the finite element predictions and the observed test failures agreed very well for all beams except for the 5-inch un-notched beams. Two explanations are possible for the over-prediction of the 5 inch un-notched beams. First, the failure location was not completely predictable for the un-notched beams. Most beams failed close to the test fixture upright but variations up to approximately 0.25 inches were seen. Second, the number of shocks required to induce failure may have started to resemble low cycle fatigue testing for some of the more robust specimen. This would have also lowered the failure levels over the predicted failure points.

**Table 5. First Passage Tests Beam Failure Summary**

| Beam Length | Notch Depth | Observed Test Failure | Predicted Failure |
|---|---|---|---|
| 5 in | None | 32.0g → 62.5g | 64.5g |
| 5 in | 0.025 in | 30.5g → 41.5g | 38.5g |
| 5 in | 0.050 in | < 27g | 18.8g |
| 3 in | None | 42.5g → 98.0g | 58.8g |
| 3 in | 0.025 in | 30.5g → 41.5g | 37.4g |
| 3 in | 0.050 in | < 27g | 20.4g |

Figure 20 shows a plot of the absorbed energy spectrum calculated from the first passage failure tests of the 5 inch beams with the 0.025-inch notch. For this test series, four beams were tested and all four beams failed on the third drop test. The three shock levels are shown in the figure: 26g, 31.5g and 41.5g which indicates that the onset of failure should be located between 31.5g and 41.5g. Ideally it would have been advantageous to uses smaller increments between tests; however, the resolution of the drop table was somewhat limited at these low levels. The failure predictions were obtained from the finite element model using a maximum strain failure criteria based on the average failure strain measured in the tensile specimen tests. The failure predictions were very good in this example with the predicted absorbed energy at failure faring through the absorbed energy spectrum from the final drop test. The vertical dashed line in Figure 20 represents the cantilever beam first resonant frequency which is the frequency line that is assumed to be predominately responsible for the beam failure, and at this frequency the absorbed energy spectra exceeds the failure prediction.

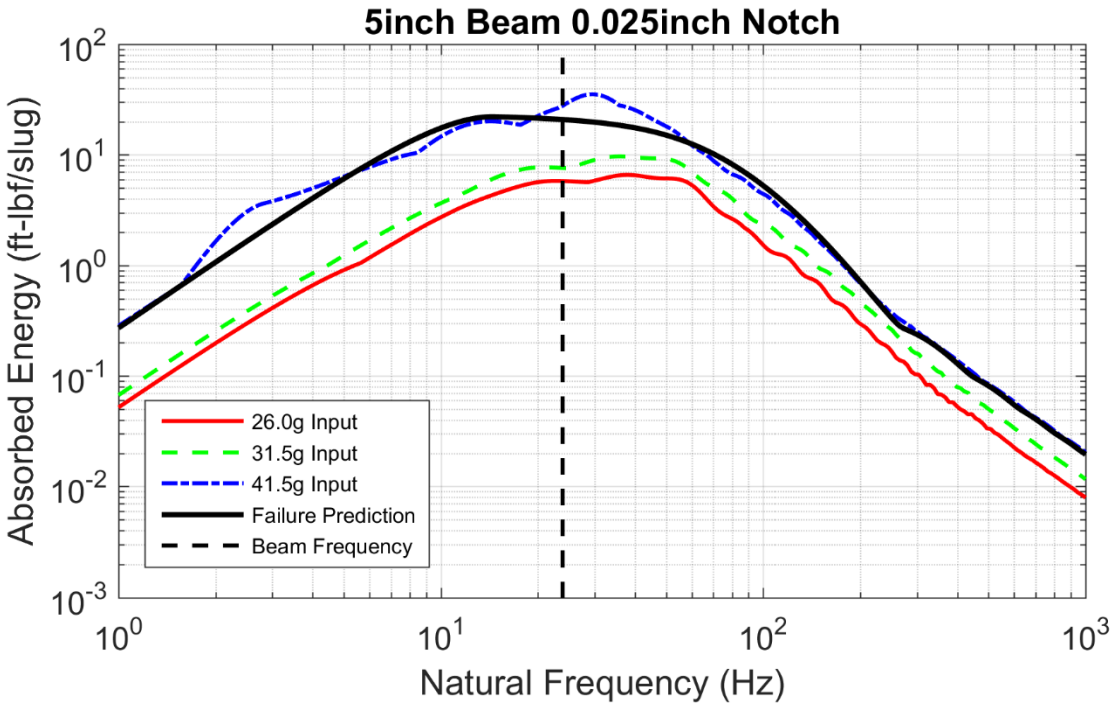


**Figure 20. 5 inch 0.025-inch Notch First Passage Failure Testing Energy Spectrum Results Compared to Failure Prediction**

Figure 21 shows a similar plot of the absorbed energy spectrum versus the predicted absorbed energy spectrum for the 3-inch-long cantilever beams with the 0.025 inch notch. As before, this test series tested four beams and all four beams failed on the third drop test. Three shock levels are shown in the figure: 21.5g, 30.5g, and 40.5g which indicate that the onset of failure is between 30.5g and 40.5g. Once again, the predicted failure was obtained from the finite element model using the peak strain failure criteria. The absorbed energy spectrum at failure again passes through the calculated absorbed energy spectrum from the last drop test. Here again, the vertical dashed line in Figure 21 represents the first resonant mode of the cantilever beam that is assumed to be predominately responsible for the failure, and at this frequency the absorbed energy spectra exceeds the failure prediction.

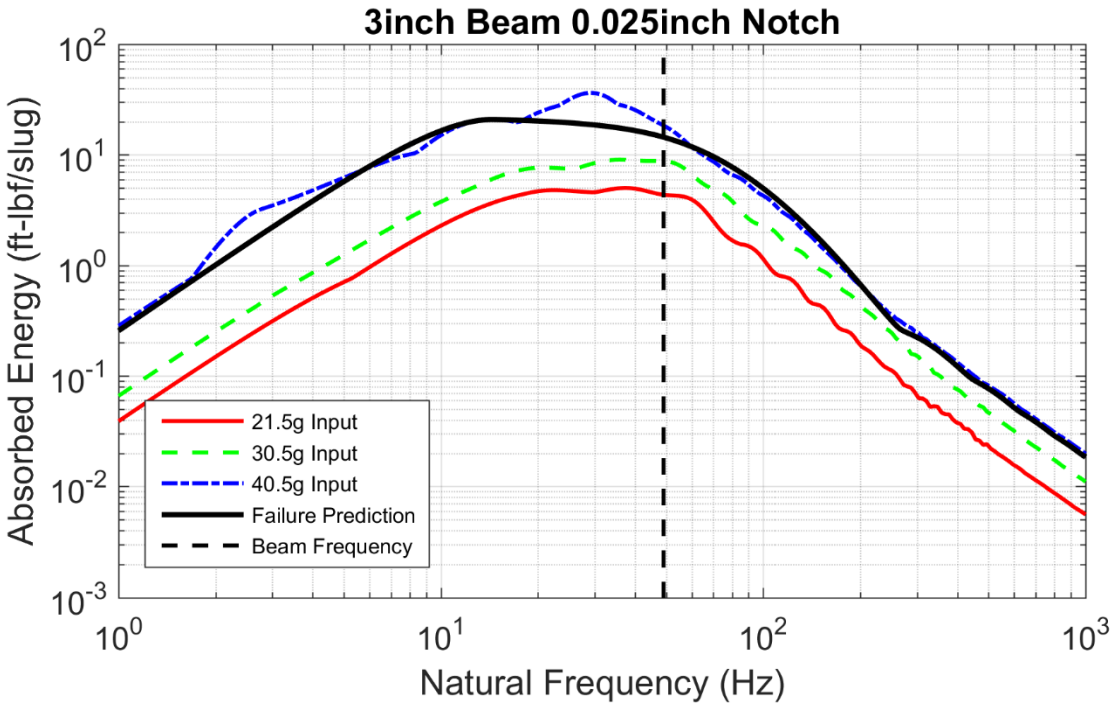


**Figure 21. 3-inch 0.025-inch Notch First Passage Failure Testing Energy Spectrum Results Compared to Failure Predictions**

One of the primary benefits of energy methods is their applicability to multiple shock scenarios. In fact, this is an often-touted advantage over traditional SRS techniques [5]. It is well known that the SRS of a time signal containing two identical shocks is the same as the SRS for one of the two shocks provided the two shocks occur sufficiently separated in time for the response to complete decay to zero. Since the SRS is a maximum response, it will not change or increase as multiple identical shock events are added to the time history. Energy spectrum techniques, in contrast, integrate over the entire time signal, adding the energy contained under the time history curve. As a result, certain energy spectrum from a signal containing two identical shocks will be twice as large as those from a single shock.

The second phase of this testing was conducted to generate a series of low-cycle fatigue failures which were analyzed using energy response spectra. The testing made use of the results from the first passage failure tests to define a shock input level near, but less than, the single shock failure point for the beams being tested. That shock input was then repeated at nominally the same level until all of the beams in the set failed. For example, the 5 in, 0.025in notched beams were tested to a nominal shock level of 31.7g which was below the failure level of 41g. The shock was repeated 27 times until all the beams failed. Some minor variability was observed between shock events due to the nature of the low levels being used on the drop table. The variability was not significant; however, it was documented and the energy spectra calculations performed here considered each shock, not simply an average of all shocks.

Table 6 presents a summary of the results from the low-cycle fatigue tests. Low cycle fatigue tests of three beam configurations were conducted. This table contains the mean shock level (which was very repeatable), the average number of hits needed to fail all the beams, and the

range of the number of shocks to fail the first and last beam in the set. The 5-inch beam with no notch was surprisingly resilient. The mean shock level was well within one standard deviation of the mean maximum shock yet all the beams withstood at least 27 44.8 g shocks. The range of hits to failure for the 3-inch beam with the 0.025-inch notch was surprisingly large, with one beam failing at the low-level shock on the first hit. The source of this variability was never confirmed, but is postulated to be from variability of the internal structure and voids in the 3-D printed beams.

**Table 6. Cantilever Beam Low-Cycle Fatigue Test Beam Failure Summary**

| Beam Length | Notch Depth | Tip Weight | Mean Shock | % of Mean Max Shock | Hits to Fail | |
|---|---|---|---|---|---|---|
| | | | | | Mean | Range |
| 5 in | None | 0.028 lbf | 44.8g | 93% | 36 | 27 → 47 |
| 5 in | 0.025 in | 0.028 lbf | 31.7g | 77% | 19 | 14 → 27 |
| 3 in | 0.025 in | 0.028 lbf | 31.5g | 78% | 12 | 1 → 18 |

In the subsequent figures the teal line is representative of the nominal shock below the single shock failure level. The red, green, and blue lines are the lowest number of shocks for failure, the mean, and the highest, respectively. The solid black line is the predicted failure from a finite element simulation of the beams. Lastly the denim colored line is the single shock failure. It is noted that for the 3-inch beam, the low-level failure was one hit. This caused the red and teal lines to overlap. However, this was below the single shock failure so the value of alpha, calculated from Basquin's equation, diverged.

Figure 22 through Figure 27 show the maximum relative kinetic energy and the maximum input energy spectra for the three beam configurations. The dotted vertical line in the figures is the fundamental frequency of the beam. The curves labeled "Single Shock Failure" are the energy spectra of the high level single shock at which the beam failed, and the curves labeled "Failure Prediction" are the energy spectra from the finite element model outputs used to predict the failure inducing shock level. Except for the 5-inch unnotched beam, the predicted failure shocks are quite good. The curve labeled "1 Shock" are the energy spectra of a single, low level shock. The mean amplitudes of theses shocks are shown in the figure legends and in Table 6. The figures show curves labeled with the number of shocks, for example "EKm @ 27 Shocks" in Figure 22. These are the summed energy spectra of the individual shocks, up to the number shown; i.e., the curve for 27 shocks is the sum of the spectra of the first 27 shocks, the one for 36 is the sum of the spectra of the first 36 shocks, etc. All the plots clearly show that the summed energy spectra are higher than the energy spectra of the single shock that broke the beams. This means that summed energy spectra are not indicative of failure.

This observation led to postulation of the power law relationship of energy spectra. The exponent, $\alpha$, was estimated from the ERS at the natural frequency of the beam configuration, i.e.,

$$E_{X1}(f_n) = E_X(f_n)N^{\alpha} \tag{52}$$

The estimated values are summarized in Table 7 for each of the beam configurations and energy response spectra. In Table 7, the terms low, mean, and high refer to the beam failures. Thus, the low values correspond to the beams that failed first while the high values refer to the beams that failed with the highest number of shocks. The values of $\alpha$ are not close to unity, which they would be true if the summed energy spectra correlated to shock failure, but they are consistent with those used in high-cycle fatigue *S-N* curves. Both the three energy spectra shown, $E_{KM}^{R}$, $E_{IM}$, seem equally good for the power law model.

**Table 7. Summary of Power Law Exponent, $\alpha$, Values**

| Beam Configuration | $E_{KM}^{R}$ | | | $E_{IM}$ | | |
|---|---|---|---|---|---|---|
| | $\alpha_{Low}$ | $\alpha_{Mean}$ | $\alpha_{High}$ | $\alpha_{Low}$ | $\alpha_{Mean}$ | $\alpha_{High}$ |
| 5 in / Unnotched | 0.33 | 0.31 | 0.28 | 0.37 | 0.34 | 0.31 |
| 5 in / 0.025 in | 0.23 | 0.21 | 0.18 | 0.31 | 0.28 | 0.25 |
| 3 in / 0.025 in | N/A* | 0.24 | 0.21 | N/A* | 0.19 | 0.17 |

* Indicates that beam failure occurred on the first shock

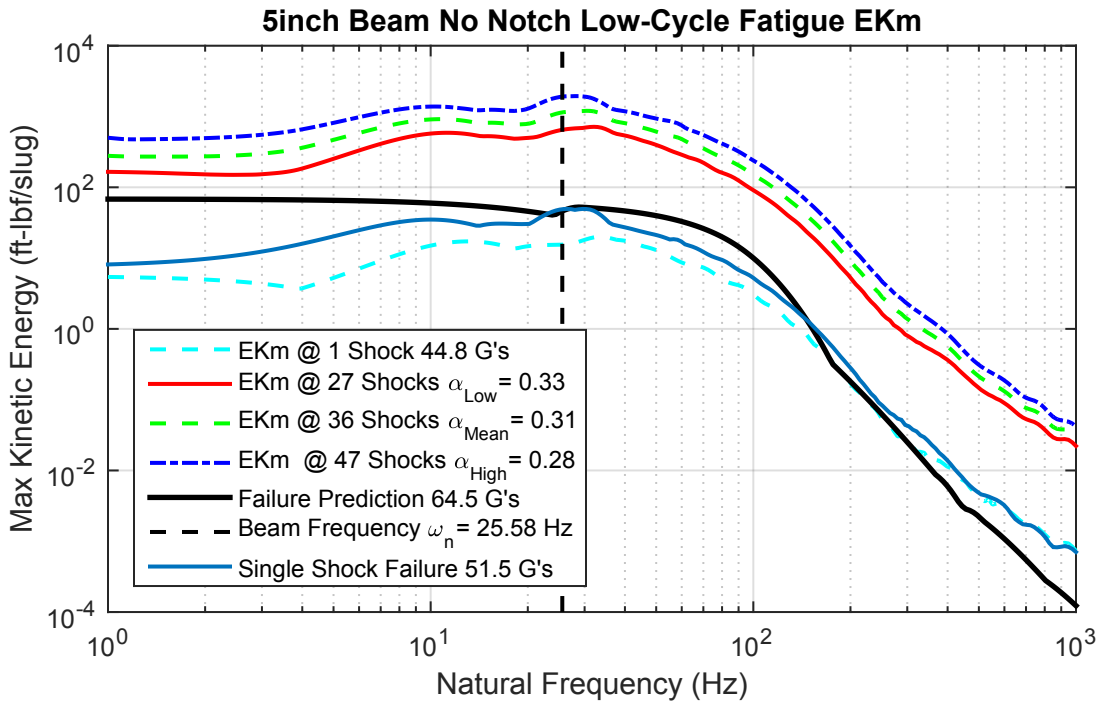


**Figure 22. Maximum Kinetic Energy Spectrum Comparison, 5 inch, Unnotched Beam**

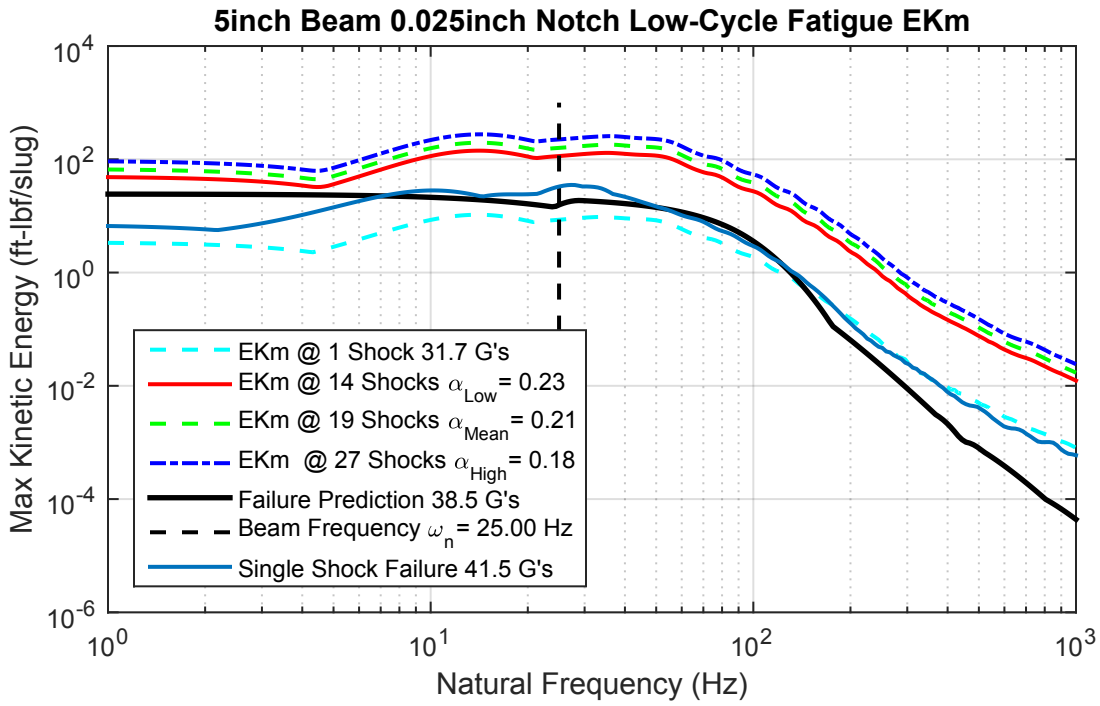


**Figure 23. Maximum Kinetic Energy Spectrum Comparison, 5-inch, 0.025-inch Notched Beam**

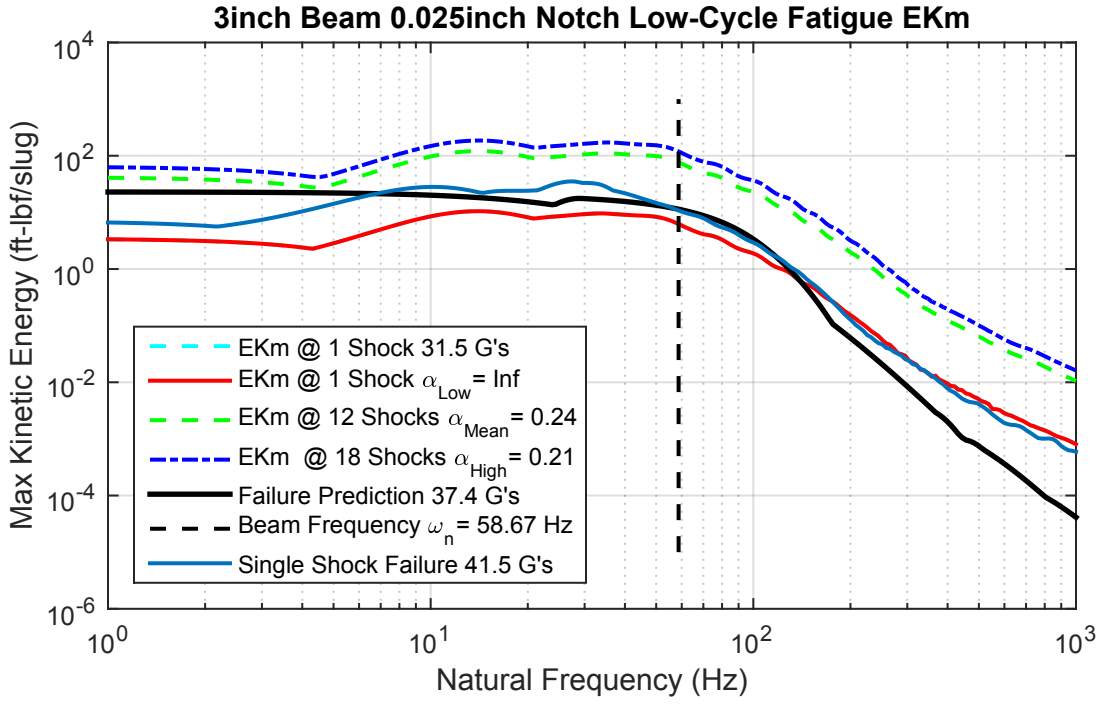


**Figure 24. Maximum Kinetic Energy Spectrum Comparison, 3-inch, 0.025-inch Notched Beam**

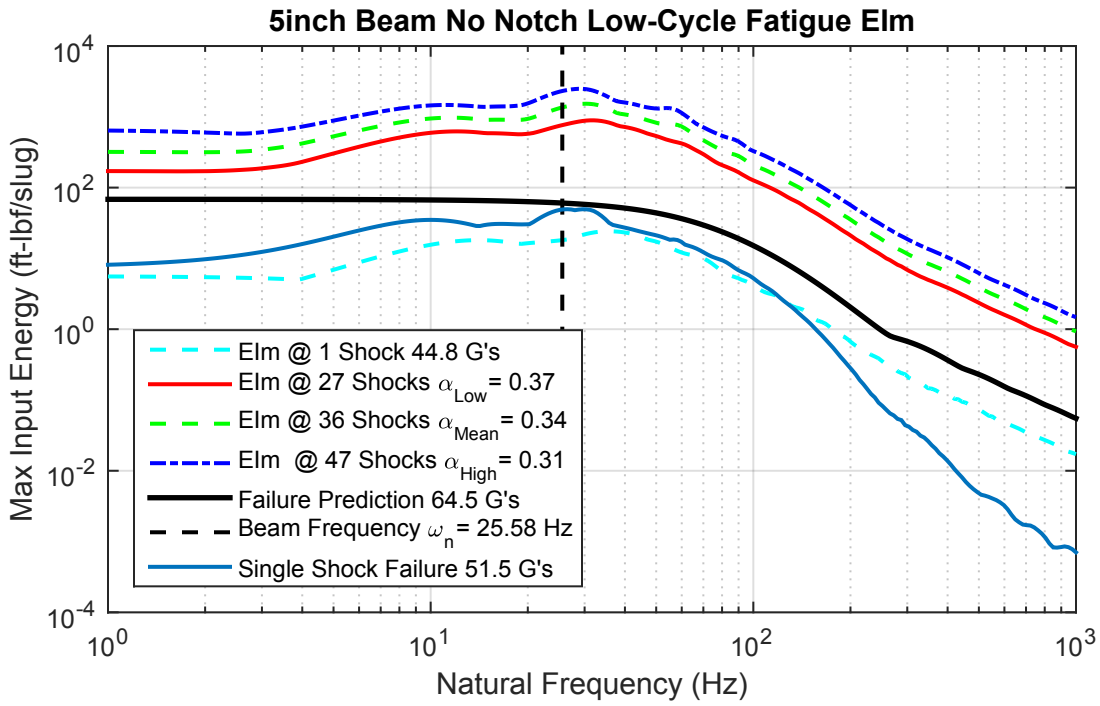


**Figure 25. Maximum Kinetic Energy Spectrum Comparison, 5 inch, Unnotched Beam**

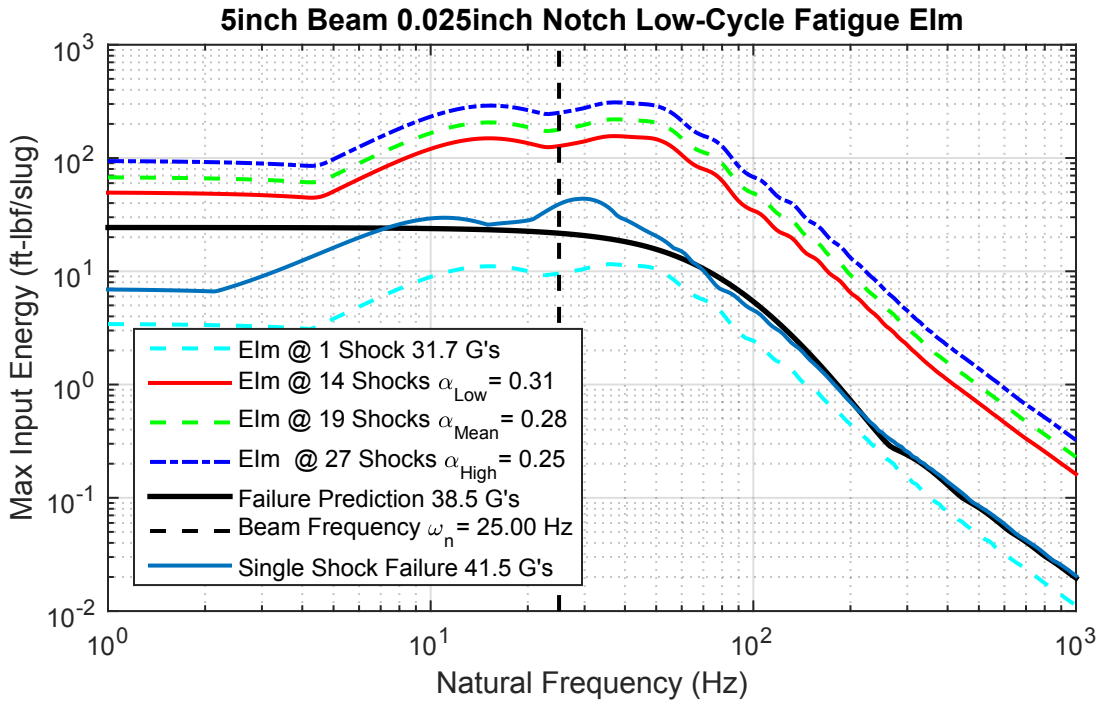


**Figure 26. Maximum Kinetic Energy Spectrum Comparison, 5-inch, 0.025-inch Notched Beam**

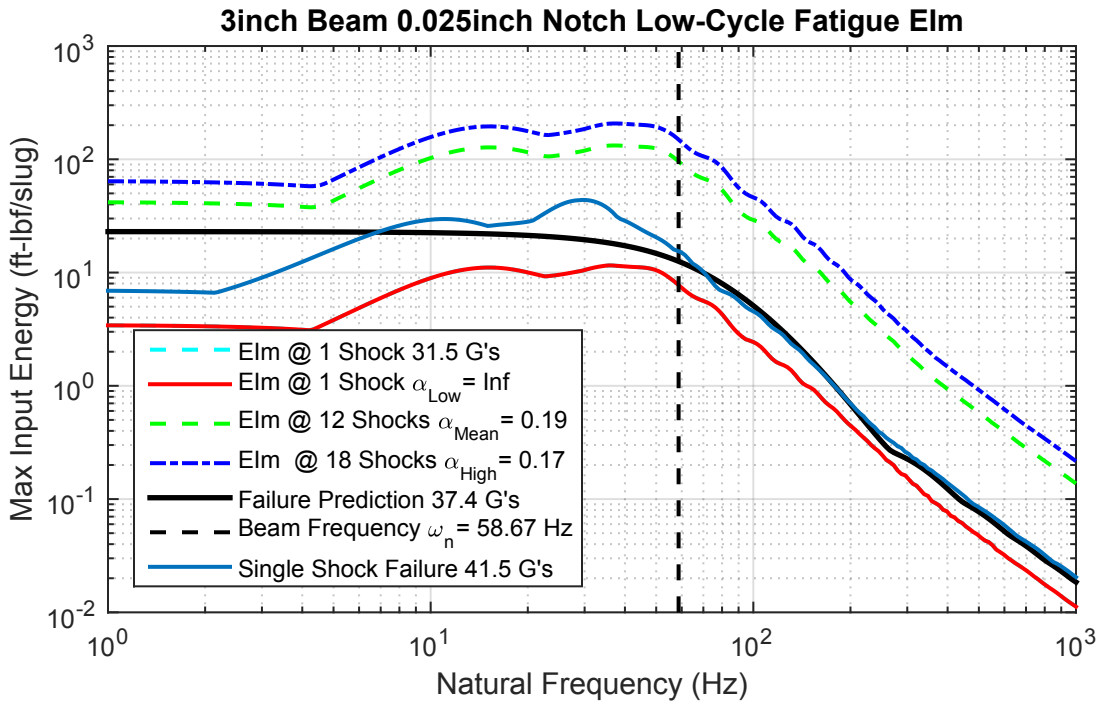


**Figure 27. Maximum Kinetic Energy Spectrum Comparison, 3-inch, 0.025-inch Notched Beam**

The results of these tests were originally documented in References [22] and [23].

An additional set of cantilever beam tests was performed on the same drop table in April 2017 using 3-D printed ABS beams printed in the length-wise raster orientation. These beams were more ductile and generally had higher failure points due to the printing orientation. However, the overall fatigue failure data were similar to the data presented here—failure was not linear with the number of shocks, but logarithmic like *S-N* data would indicate.

# 8. CANTILEVER BEAM 6-DOF SHAKER SHOCK TEST RESULTS

A second round of testing was performed on the SNL/NM large 6-DOF shaker in Tech Area III in December 2015. For this testing, a total of 68 3-D printed cantilever beams were tested. The cantilever beams used for this investigation were again made of ABS plastic and printed by the Sandia National Laboratories Additive Manufacturing group. A photograph of the test setup is shown in Figure 28. The tests were conducted using 17 sets of four beams per test. Initial tests were performed by incrementally stepping up the input shock load until all four beams failed. Typically, most beams failed after a few shocks. The second round of testing attempted to quantify low-cycle fatigue failures for cantilever beams of the same design. For the low-cycle fatigue tests, a test level less than the failure level was selected and that test was repeated until all beams failed—sometimes this was a few shocks, sometimes hundreds of shocks.

Figure 29 is close-up photograph of a set of three-inch-long cantilever beams installed in the test fixture. Testing was performed on both three-inch and five-inch-long cantilever beams for this study. Also shown in this figure are a set of the steel clamp-on collar weights and the stress concentration notch near the base of the cantilever beam.

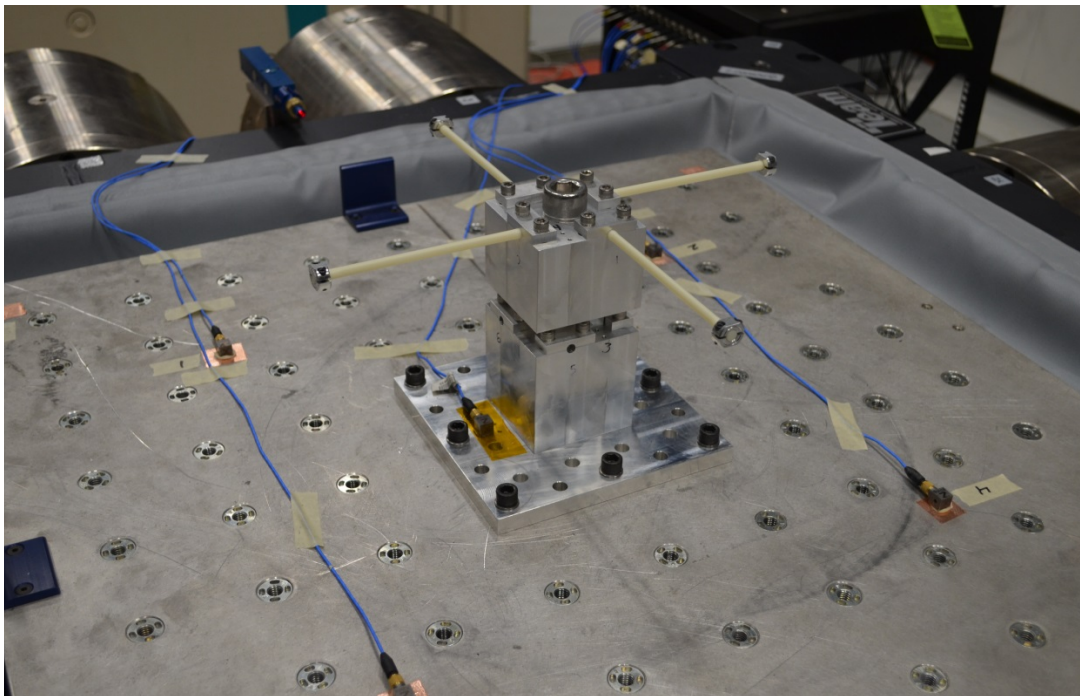

**Figure 28. Cantilever Beam Test Fixture and Test Specimen Installed on the 6-DOF Shaker Table**

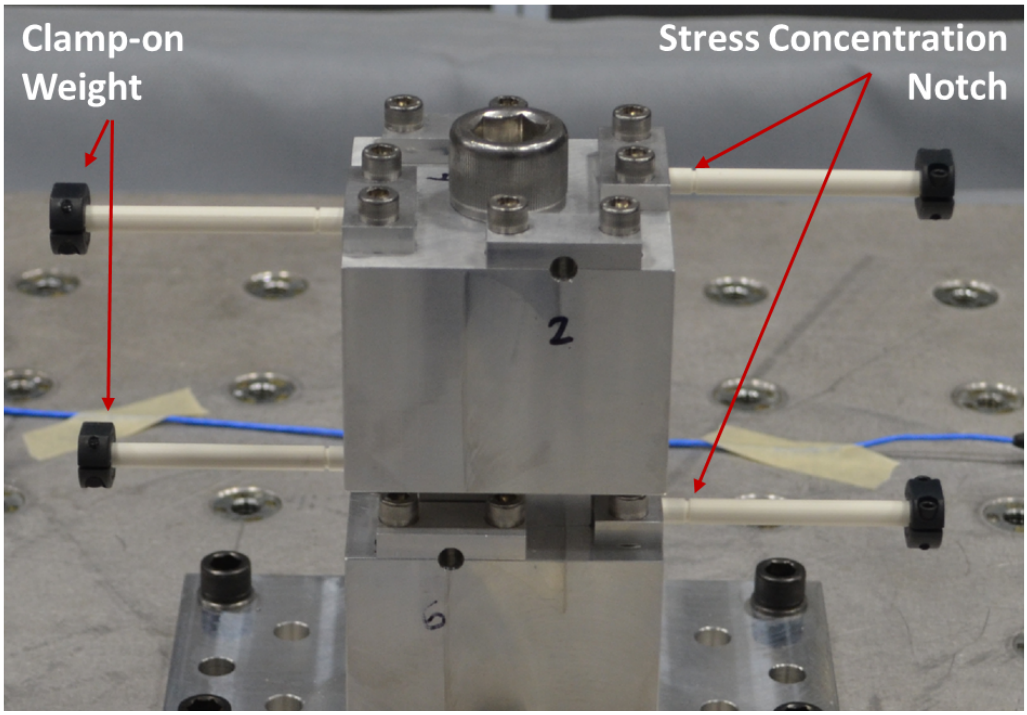


**Figure 29. Photograph of the Test Fixture with 3-D Printed Cantilever Beams Installed Showing the Clamp-on Collar Weights and the Stress Concentration Notch**

Instrumentation for this test consisted of five tri-axial accelerometers, one mounted on the upright fixture base, and the other four mounted near each of the four corners of the table as shown in Figure 28. As a result, only the base input to the system was recorded; however, the four corner accelerometers do allow for measurements of the table rotations.

Figure 30 shows a plot of a typical translational acceleration time history from a shock event on the 6-DOF shaker. The acceleration shown is the table average acceleration input in each direction which is essentially identical to the recorded acceleration at the fixture base. There are some minor differences since the fixture base accelerometer was located slightly off-center due to the need to center the fixture on the table. Figure 31 shows a plot of a typical rotational acceleration time history from the same shock event. The rotational acceleration time histories had to be derived from the tri-axial accelerometers at the four corners of the table. For this analysis, it was assumed that the table's center of rotation was coincident with the table's geometric center. While the resulting calculations indicated that this was not universally true, the difference was found to be very small and thus it was ignored for this analysis.

Figure 32 and Figure 33 show the calculated pseudo-velocity SRS data for the three translational table inputs and the three rotational table inputs, respectively. As can be seen in Figure 32, the translational spectra are nearly identical and in Figure 33, two of the three rotational spectra are very close while the z-axis rotation spectrum is certainly in-family.

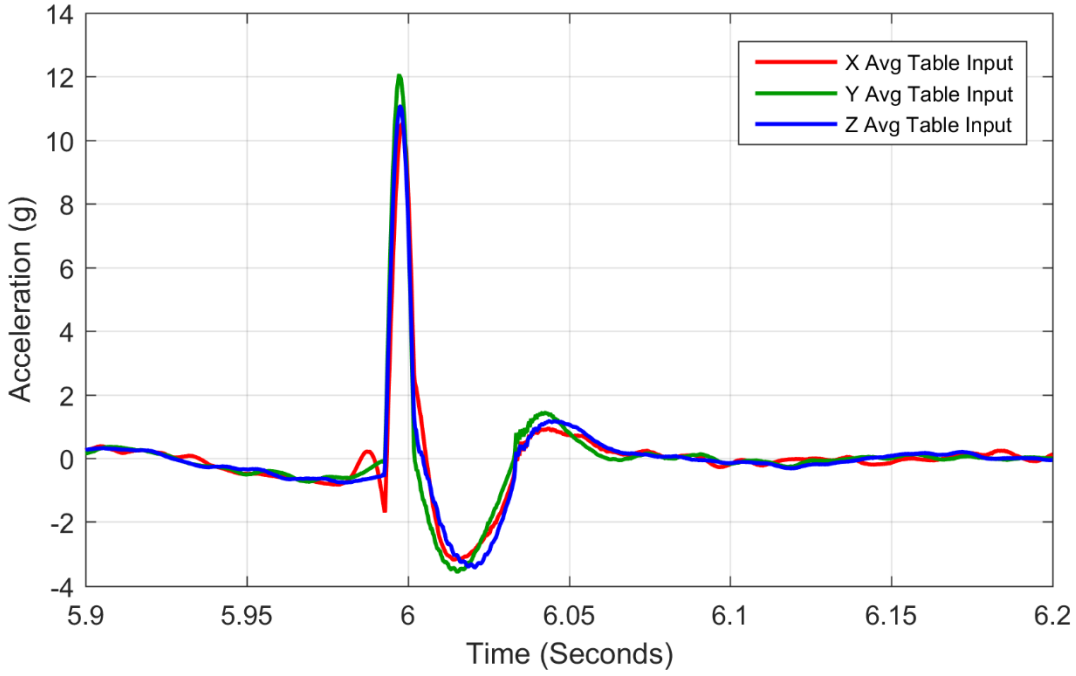


**Figure 30. Typical Translational Acceleration Profile from 6-DOF Shaker Shock Tests**

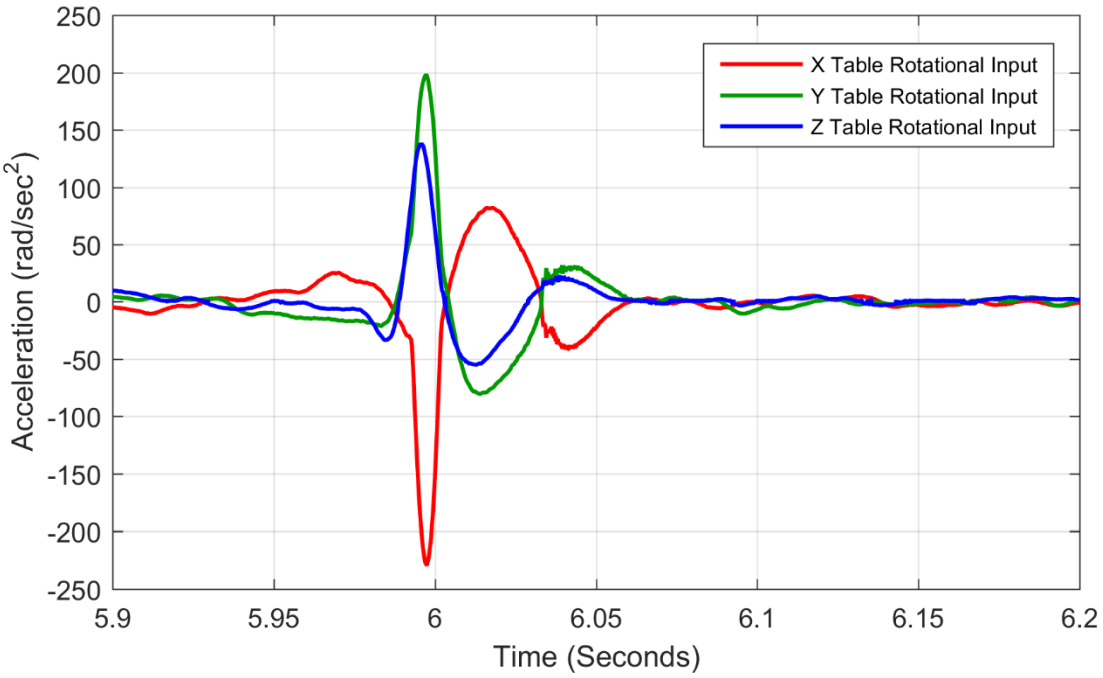


**Figure 31. Typical Rotational Acceleration Profile from 6-Dof Shaker Shock Tests**

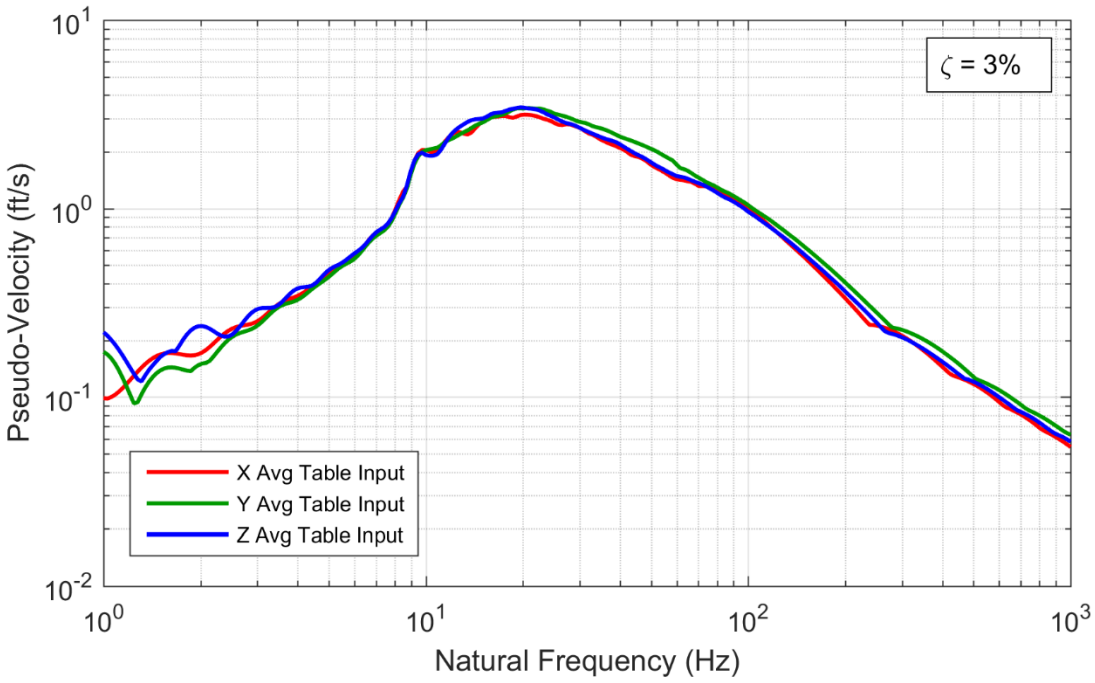


**Figure 32. Typical Translational Pseudo-Velocity SRS from 6-DOF Shaker Shock Tests**

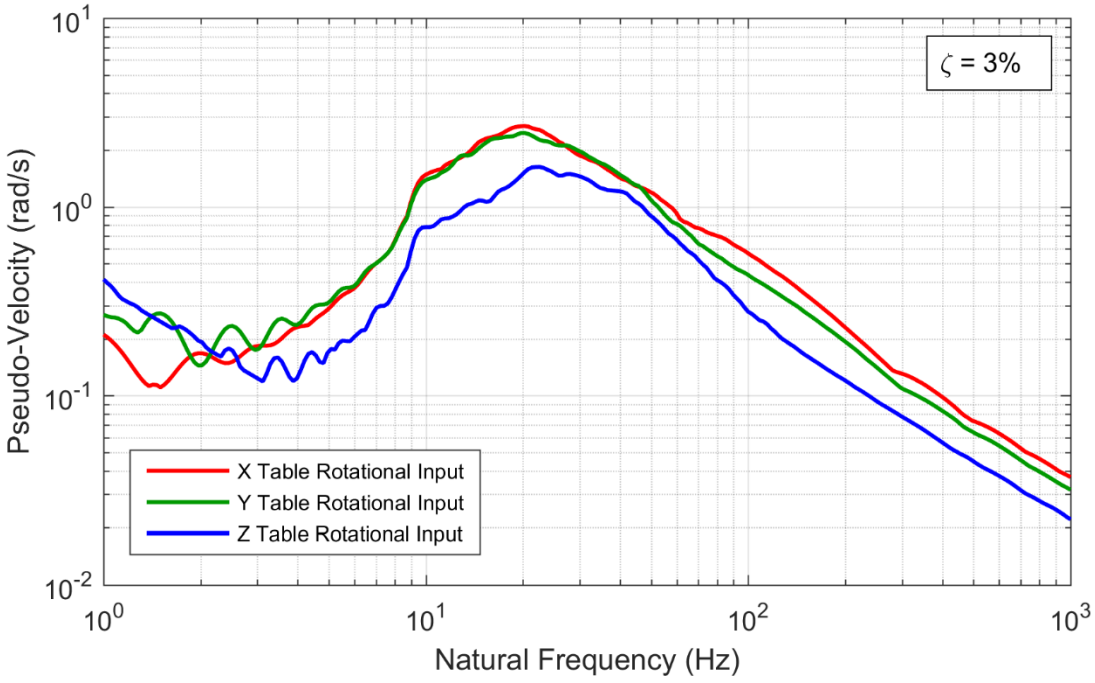


**Figure 33. Typical Rotational Pseudo-Velocity SRS from 6-DOF Shaker Shock Tests**

A total of 3,424 shocks were performed on the 6-DOF shaker table divided among 17 separate test series. Of these tests, all failures were brittle failures due to the crosswise raster orientation of the 3-D printed beams. However, it was noticed that many beams cracked before failure but the crack was not always readily propagated through the cross-section. It appeared from observations of the testing, that some beams would crack sufficiently far through the cross-section to lower their fundamental natural frequency to be outside of the excitation frequency range of the test. At that point, it became very difficult to propagate the crack through the intact portion of the beam and it would often take many shocks to completely fail the beam.

To ensure that reasonable failure predictions could be made, a series of quasi-static pull tests were performed on tensile coupons printed alongside the test specimen. Printing the coupons along with the beams ensured material properties for each lot could be obtained for use in analyses. As was previously discussed, the raster orientation can be used to tailor the failure mechanism to be either ductile or brittle. For this set of test specimen, the crosswise raster orientation was intentionally selected to create a brittle beam failure.

The 6-DOF shaker shock tests were conducted by applying a shock load simultaneously in all six degrees of freedom (three translations and three rotations). The shock load was applied once at each level and the levels were incrementally increased until all the cantilever beams failed. Most beam sets either failed all at once or on adjacent shocks indicating that the failure levels were reasonably consistent for all components of the same design. Figure 34 shows a plot of all six pseudo-velocity SRS curves overlaid on the same graph together with the SRS for a single degree-of-freedom haversine shock predicted to fail the cantilever beam. The beams tested here were all five-inch-long 0.25-inch diameter round rods with a 0.025-inch-deep notch near the base of the beam and a single steel collar positioned at the free end. The SRS results shown in Figure 34 resulted in the simultaneous failure of the last three beams from a four beam test series. The failure prediction was derived from a dynamic finite element model, tensile test data to determine the strain at failure, and correlated with previously performed drop table testing. As can be seen in Figure 34, all the individual axis SRS curves are well below the single axis failure. However, the combination of the 6-DOF shock resulted in failure.

Figure 35 shows the composite pseudo-velocity SRS derived using the methods presented in Section 2.3 for the same shock data shown in Figure 34 together with the single axis failure and a line designating the beam's fundamental bending frequency. Here, the failure occurs because the composite SRS extends above the failure prediction at the beam's fundamental mode even though the bulk of the test data SRS is well below the predicted failure SRS.

Likewise, the composite 6-DOF maximum absorbed energy spectrum is shown in Figure 36 along with the maximum absorbed energy spectrum SDOF failure prediction. As was shown previously, the absorbed energy spectrum follows the pseudo-velocity SRS and shows the same result. Failure is assumed to have occurred because the energy at the beam's first natural frequency exceeds the SDOF failure prediction even though the bulk of the energy spectrum falls below the SDOF prediction. A similar result is shown in Figure 37 for the composite 6-DOF input energy. It was previously hypothesized that the input energy would require the same composite 6-DOF methodology as the absorbed energy and the results shown in Figure 37 seem to show that this relationship holds.

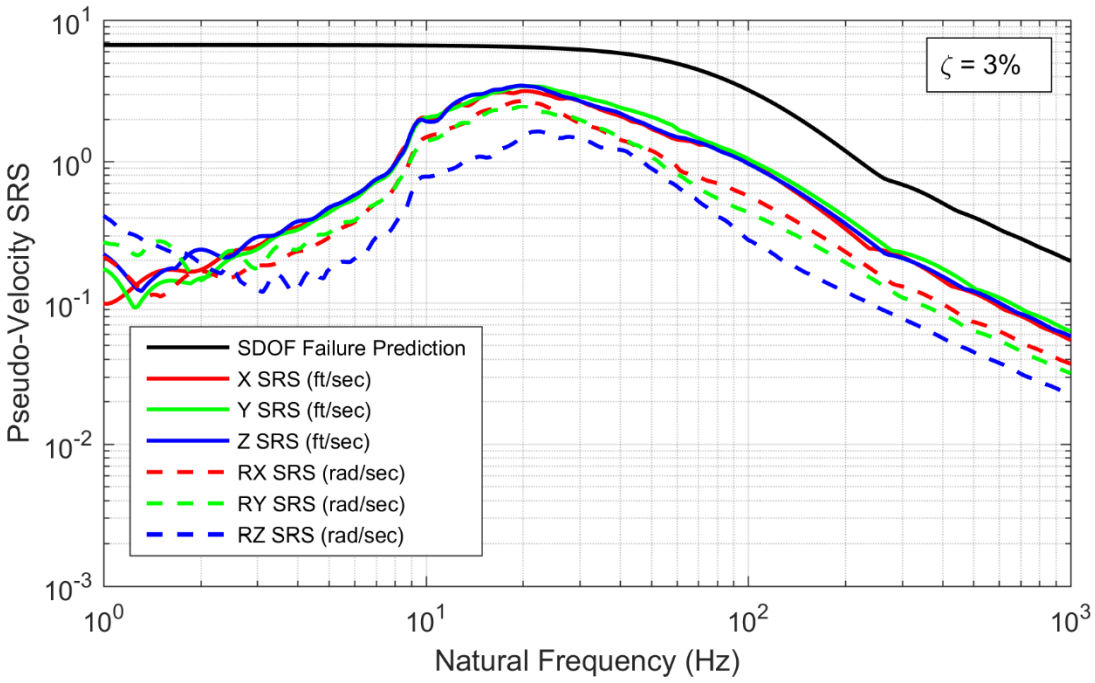


**Figure 34. Pseudo-Velocity SRS Comparison of Individual 6-DOF SRS with Single Axis Haversine Shock Failure Prediction SRS**

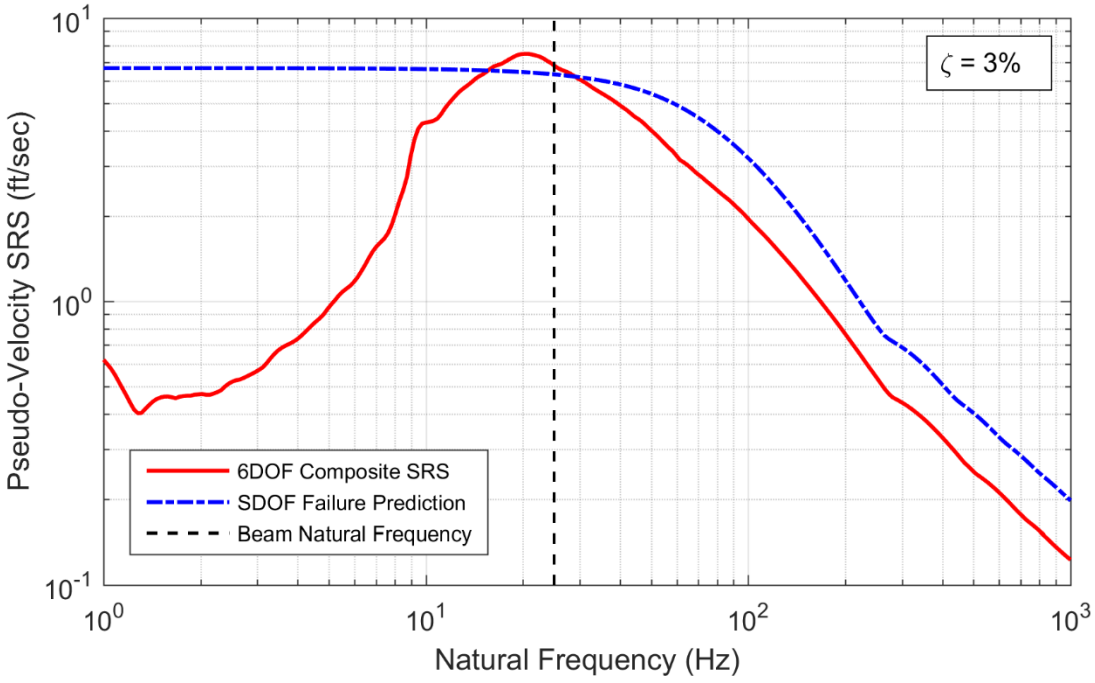


**Figure 35. Pseudo-Velocity SRS Comparison of 6-DOF Composite SRS with Single Axis Haversine Shock Failure Prediction SRS**

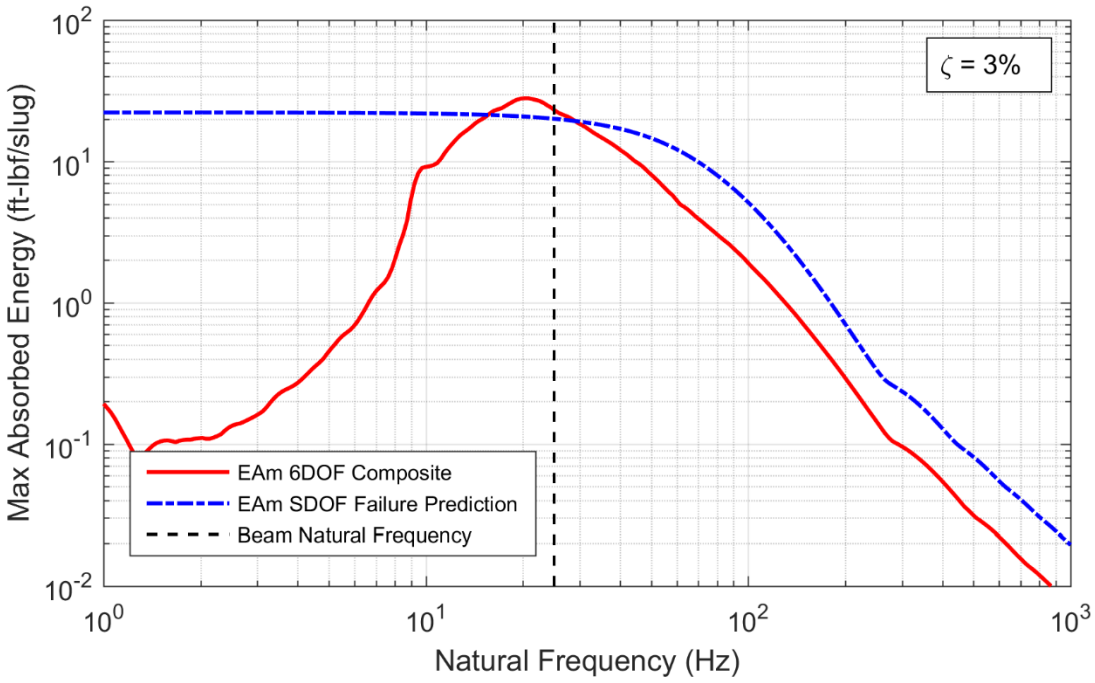


**Figure 36. Maximum Absorbed Energy Spectrum Comparison of 6-DOF Composite Spectrum with Single Axis Haversine Shock Failure Prediction**

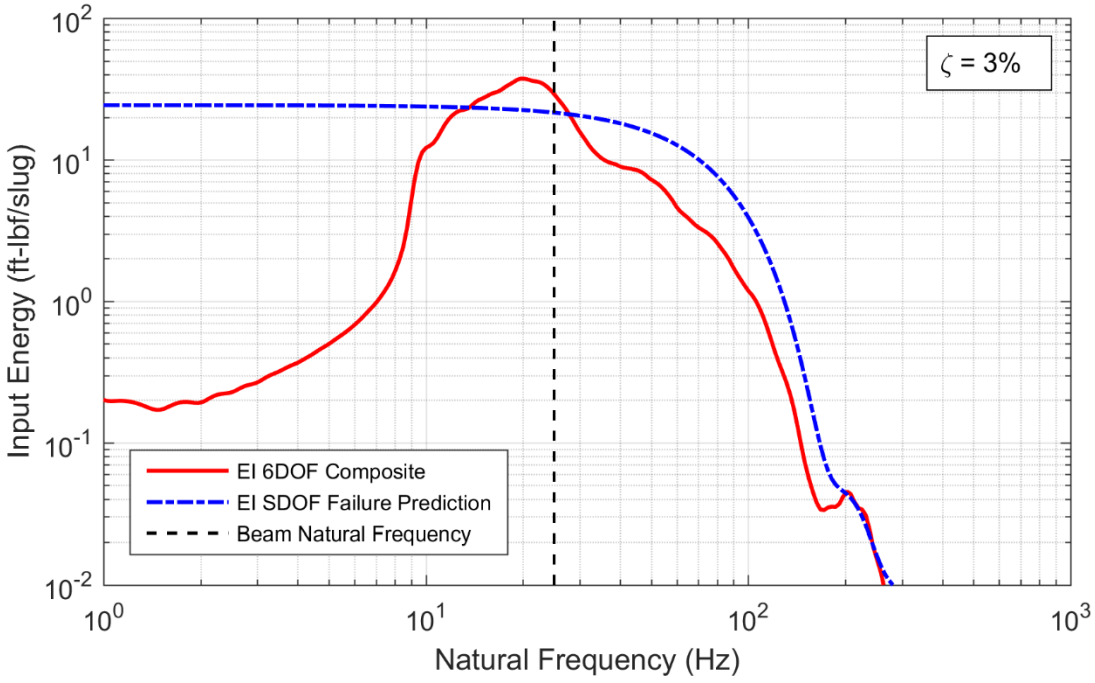


**Figure 37. Maximum Absorbed Energy Spectrum Comparison of 6-DOF Composite Spectrum with Single Axis Haversine Shock Failure Prediction**

An alternate method for deriving the margin at failure using the energy methods can also be readily calculated if the modal data from the component is available. Since the component under test is a cantilever beam, modal data is readily extracted from a simple finite element model. Table 8 shows the first five calculated natural frequencies and percent modal mass in the x- and y-direction for a five-inch cantilever beam with a steel tip weight and a 0.025-inch notch. As expected, the first bending mode is relatively low frequency and contains the bulk of the modal mass for the system. The modal mass diminishes rapidly for the second, third, and fourth bending mode as shown. Finally, the first axial mode appears as mode five in the system.

**Table 8. Calculated Natural Frequencies and Modal Masses for a 5inch 0.025inch Notch Cantilever Beam with One Steel Tip Weight**

| Mode | Frequency (Hz) | X-direction (Axial) Percent Modal Mass | Y-direction (Transverse) Percent Modal Mass |
|---|---|---|---|
| 1 | 23.9 | 0.0 | 68.0 |
| 2 | 362 | 0.0 | 5.58 |
| 3 | 1174 | 0.0 | 1.65 |
| 4 | 2458 | 0.0 | 0.77 |
| 5 | 2778 | 18.95 | 0.0 |

Table 9 lists the predicted energy required to cause beam failure in a single axis bending test. The results shown in this table were derived by interpolating the predicted input and maximum absorbed energy spectra shown previously at each of the bending frequencies. A plot of the dissipated energy spectrum is not shown but is readily obtained and values extracted. Table 10 shows the predicted energy required to cause beam failure in a single axis axial test. The axial failure energies are significantly higher than the bending energies as expected. To obtain the SDOF failure energies for the axial case, a separate finite element load case was run with an axial shock applied instead of the transverse shock. As expected, the lowest modes contain the highest energies with the energies significantly tapering off at the higher modes.

**Table 9. Energy Required for SDOF Bending Failure of the 5inch 0.025inch Notch Beam with One Steel Tip Weight at the First Five Modes**

| Mode | SDOF Failure Input Energy (ft-lbf/slug) | SDOF Failure Max Absorbed Energy (ft-lbf/slug) | SDOF Failure Dissipated Energy (ft-lbf/slug) |
|---|---|---|---|
| 1 | 21.74 | 20.23 | 8.28 |
| 2 | 4.031E-3 | 0.164 | 4.022E-3 |
| 3 | 1.019E-4 | 1.417E-2 | 1.019E-4 |
| 4 | 1.098E-5 | 3.222E-3 | 1.098E-5 |
| 5 | 7.595E-6 | 2.520E-3 | 7.595E-6 |

**Table 10. Energy Required for SDOF Axial Failure of the 5inch 0.025inch Notch Beam with One Steel Tip Weight at the First Five Modes**

| Mode | SDOF Failure Input Energy (ft-lbf/slug) | SDOF Failure Max Absorbed Energy (ft-lbf/slug) | SDOF Failure Dissipated Energy (ft-lbf/slug) |
|---|---|---|---|
| 1 | 8.70E+5 | 8.09E+5 | 3.31E+5 |
| 2 | 1.61E+2 | 6.57E+3 | 1.61E+2 |
| 3 | 4.077 | 5.67E+2 | 4.08 |
| 4 | 0.439 | 1.29E+2 | 0.438 |
| 5 | 0.304 | 1.01E+2 | 0.304 |

To compare these failure energies against the test, the normalized energy margin equation given in Equation (25) is recast to include the rotational shock energy terms and given in Equation (53).

$$ModeMargin = \frac{E_x}{E_{x\,fail}} + \frac{E_y}{E_{y\,fail}} + \frac{E_z}{E_{z\,fail}} + \frac{l^2 E_{RY}}{E_{y\,fail}} + \frac{l^2 E_{RZ}}{E_{z\,fail}} + \frac{h^2 E_{RX}}{E_{y\,fail}}. \quad (53)$$

In Equation (53), the term $l$ is the distance from the table's center of rotation to the beam center of mass and $h$ are the distance from the table surface to the beam centerline.

Table 11 lists the input energies from each of the 6-DOF shock inputs at each of the first five modes. The input energy numbers from Table 11 can be substituted into Equation (18) along with the failure energies from Table 9 and Table 10 to determine the modal margin value. Similarly, Table 12 lists the maximum absorbed energies and Table 13 lists the dissipated energies from each of the 6-DOF shock inputs at each of the first five modes. The desire is to compare the results of the normalized energy summation in Equation (53) with the actual failure seen in the 6-DOF shock testing to determine which of the three energy types best correlates to the failures seen.

**Table 11. Input Energy Supplied per Mode During 6-DOF Shock of 5inch 0.025inch Notch Beam with One Steel Tip Weight**

| Mode | X Shock (ft-lbf/slug) | Y Shock (ft-lbf/slug) | Z Shock (ft-lbf/slug) | RX Shock (lbf/slug-ft) | RY Shock (lbf/slug-ft) | RZ Shock (lbf/slug-ft) |
|---|---|---|---|---|---|---|
| **1** | 5.947 | 7.198 | 6.121 | 3.765 | 3.533 | 1.701 |
| **2** | 9.63E-4 | 1.21E-3 | 8.13E-4 | 2.95E-4 | 1.70E-4 | 7.38E-5 |
| **3** | 2.36E-5 | 2.74E-5 | 1.54E-5 | 9.41E-6 | 8.01E-6 | 1.68E-5 |
| **4** | 4.12E-6 | 2.57E-6 | 1.62E-6 | 3.64E-6 | 1.59E-5 | 1.14E-5 |
| **5** | 1.27E-6 | 1.29E-6 | 1.00E-6 | 7.49E-7 | 1.55E-6 | 4.32E-6 |

**Table 12. Maximum Absorbed Energy Supplied per Mode During 6-DOF Shock of 5inch 0.025inch Notch Beam with One Steel Tip Weight**

| Mode | X Shock (ft-lbf/slug) | Y Shock (ft-lbf/slug) | Z Shock (ft-lbf/slug) | RX Shock (lbf/slug-ft) | RY Shock (lbf/slug-ft) | RZ Shock (lbf/slug-ft) |
|---|---|---|---|---|---|---|
| **1** | 4.370 | 5.455 | 4.963 | 2.920 | 2.469 | 1.235 |
| **2** | 1.41E-2 | 1.91E-2 | 1.50E-2 | 6.13E-3 | 4.28E-3 | 2.01E-3 |
| **3** | 1.08E-3 | 1.42E-3 | 1.19E-3 | 4.83E-4 | 3.63E-4 | 1.75E-4 |
| **4** | 2.41E-4 | 3.18E-4 | 2.67E-4 | 1.11E-4 | 8.25E-5 | 4.08E-5 |
| **5** | 1.89E-4 | 2.49E-4 | 2.09E-4 | 8.73E-5 | 6.49E-5 | 3.17E-5 |

**Table 13. Dissipated Energy Supplied per Mode During 6-DOF Shock of 5inch 0.025inch Notch Beam with One Steel Tip Weight**

| Mode | X Shock (ft-lbf/slug) | Y Shock (ft-lbf/slug) | Z Shock (ft-lbf/slug) | RX Shock (lbf/slug-ft) | RY Shock (lbf/slug-ft) | RZ Shock (lbf/slug-ft) |
|---|---|---|---|---|---|---|
| **1** | 5.946 | 7.197 | 6.120 | 3.764 | 3.532 | 1.701 |
| **2** | 9.63E-4 | 1.21E-3 | 8.129E-4 | 2.945E-4 | 1.70E-4 | 7.36E-5 |
| **3** | 2.35E-5 | 2.73E-5 | 1.54E-5 | 9.37E-6 | 7.97E-6 | 1.67E-5 |
| **4** | 4.04E-6 | 2.54E-6 | 1.61E-6 | 3.55E-6 | 1.54E-5 | 1.11E-5 |
| **5** | 1.25E-6 | 1.28E-6 | 9.93E-7 | 7.36E-7 | 1.51E-6 | 4.16E-6 |

Using the input, maximum absorbed, and dissipated energies listed in Table 11, Table 12, and Table 13 together with the SDOF failure energies from Table 9 and Table 10 along with Equation 19, the normalized energy at each mode for each of the three energy types is calculated and presented in Table 14. According to the energy theory, the failure should occur when the normalized energy exceeds unity. As can be seen from Table 14 the normalized energies are not exactly conclusive. The mode four normalized energies are all out of line with the other four mode energies. It is suspected that the mode four energies are a result of numerical errors from the division of very small numbers. Referring to Table 8, the mode four modal mass is less than one percent and should probably be eliminated from consideration. Summing the normalized input energies from Table 14 for modes 1, 2, 3, and 5 equals 1.846. Likewise, the summation of normalized maximum absorbed energies for the same four modes is 1.085. Finally, the normalized dissipated energy summation for the same four modes is 3.063. While clearly these metrics exceed the failure criteria, only the maximum absorbed energy is close to the failure criteria. Give the modal masses for the cantilever beam, it is expected that failure will be a combination of the lowest modes with the highest modal mass participation factor—modes 1, 2, 3, and 5 in this case. Since the testing performed here stepped up until failure, it is obvious that the normalized energy summation should be close to but slightly greater than unity. Therefore, both the summation of the normalized input energy and normalized dissipated energy appear to be relatively poor predictors of failure for the shock scenario. On the other hand, the summation of normalized maximum absorbed energy is very close to unity but slightly above as should be expected.

**Table 14. Normalized Energy per Mode from 6-DOF Testing of the 5inch 0.025inch Notch Beam with One Steel Tip Weight at the First Five Modes**

| Mode | Normalized Input Energy (ft-lbf/slug) | Normalized Max Absorbed Energy (ft-lbf/slug) | Normalized Dissipated Energy (ft-lbf/slug) |
|---|---|---|---|
| 1 | 0.7503 | 0.6276 | 1.9687 |
| 2 | 0.5694 | 0.2409 | 0.5704 |
| 3 | 0.5262 | 0.2161 | 0.5243 |
| 4 | 1.1139 | 0.2131 | 1.0892 |
| 5 | 1.79E-5 | 7.20E-6 | 1.76E-5 |

Following the initial testing, low-cycle fatigue testing was performed by selecting a shock test level less than the determined failure load and repeating that shock until all beams in the set failed. A different shock input level was then selected and the test repeated. From the data collected, a composite input energy spectrum was calculated for each shock as detailed previously and the sum of the input energy from all shocks experienced by a given cantilever beam was calculated. Figure 38 shows a plot of the total input energy compared to the number of shocks to failure from the elliptic cantilever beam tests. The slope of the least squares fit straight line through the data is 0.65 which is nearly identical to the predicted slope of 0.64 for common structural materials, derived in Section 3.1. While it is interesting that the measured slope and the theoretical slope are very close, it is somewhat coincidental since the theoretical slope is derived from a nominal value for common structural materials and not ABS specifically. However, it is significant that the slope is in-family with structural materials and not substantially different.

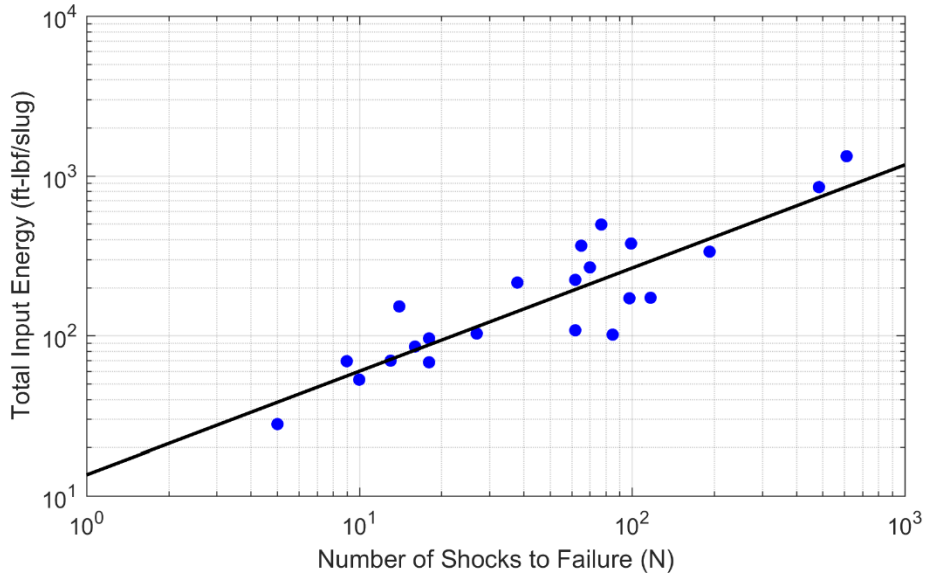


**Figure 38. Plot of Number of Shocks to Failure versus Total Input Energy from 6-DOF Cantilever Beam Tests**

Figure 39 shows a plot of the same elliptic beam 6-DOF fatigue test data, this time formatted to show the number of shocks to failure compared to the average input energy per shock. Since all of the shock events for a single test series were nominally the same, the input energy from all the shocks was averaged. The slope of the least squares fit straight line through the data is −0.35 which is again nearly equal to the predicted slope of −0.36 for common structural materials derived in Section 3.1. Here again, the significance is not in the closeness of the result exactly but rather that the result is in-family with general structural materials, confirming the fatigue relationships derived here for input energy are similar to the more common *S-N* curve results with similar Basquin equation exponents.

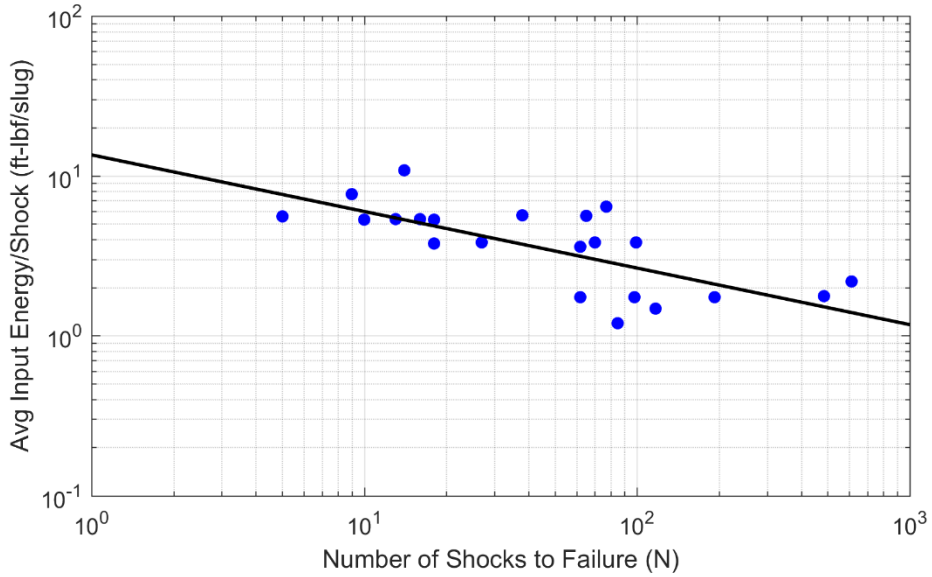


**Figure 39. Plot of Number of Shocks to Failure versus Average Input Energy from 6-DOF Cantilever Beam Tests**

These test results show that a power-law relationship between input energy and number of cycles was derived for high and low-cycle fatigue. This relationship was extended to low-cycle shock fatigue. The equation, like the traditional *S-N* relationship, depends on experimental data to define empirical coefficients. The resulting empirically determined coefficients were in-family with those determined for most general structural materials.

The results from these tests were originally documented in References [24] and [25].

# 9. CANTILEVER BEAM SDOF SHAKER SHOCK TEST RESULTS

One of the primary goals of this test series was to repeat some of the tests performed on the 6-DOF shaker table. Part of the reason for this was to ensure that analogous results were obtained from single axis testing and multi-axis testing. In addition, since it was necessary to derive the theory for composite energy spectra for 6-DOF testing, there were some additional question as to accuracy and applicability of the results. This questioning follows along with the current understandable uncertainty surrounding testing on 6-DOF shakers versus SDOF shakers in general.

It should also be noted again that new 3-D printed beams were obtained for the SDOF testing in the CDL since the previous batch of cantilever beams had all been broken. The beams used for this test series were all 5-inch round beams with the 0.025-inch notch at the base. As such, some discrepancy between these results and the 6-DOF results using the elliptic cross-section beams is expected.

Since the CDL testing made use of a smaller shaker, it was not possible to recreate the classical shocks used on the drop table or the closer approximations obtained on the large 6-DOF shaker. Rather, an oscillating shock was used with a sample acceleration time history shown in Figure 40.

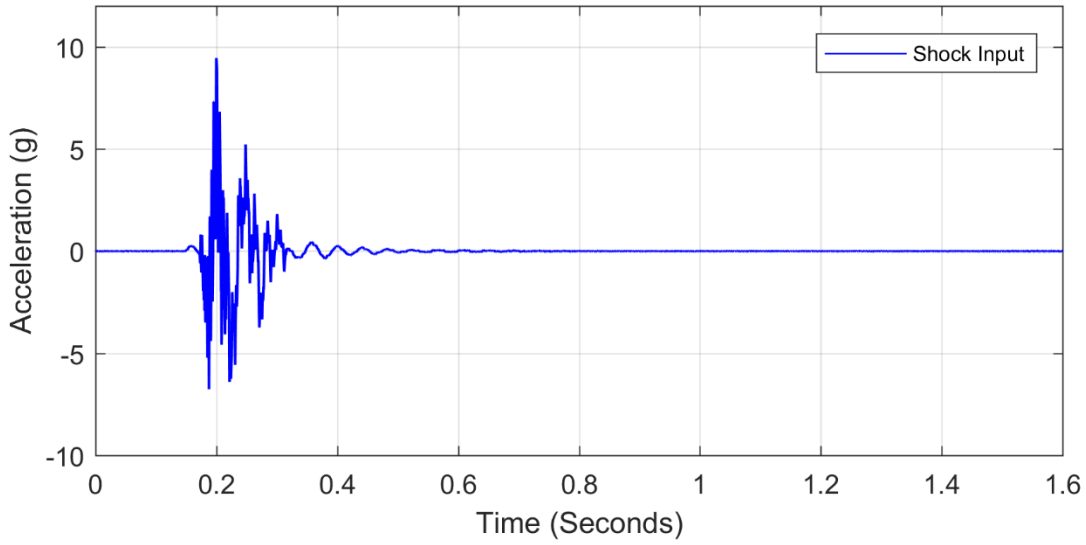


**Figure 40. Sample Shock Input for CDL Testing**

The intention was to perform low-cycle fatigue testing on the cantilever beams; however, several of the shock test levels were considerably lower than previously used and some of the shock testing crossed the line into the high-cycle fatigue regime. Figure 41 shows a plot of the total input energy compared to the number of shocks to failure from the CDL testing of the round cantilever beams. The slope of the least squares fit straight line through the data is 0.707 which is very similar to the measured 6-DOF slope of 0.65 and the theoretical slope of 0.64.

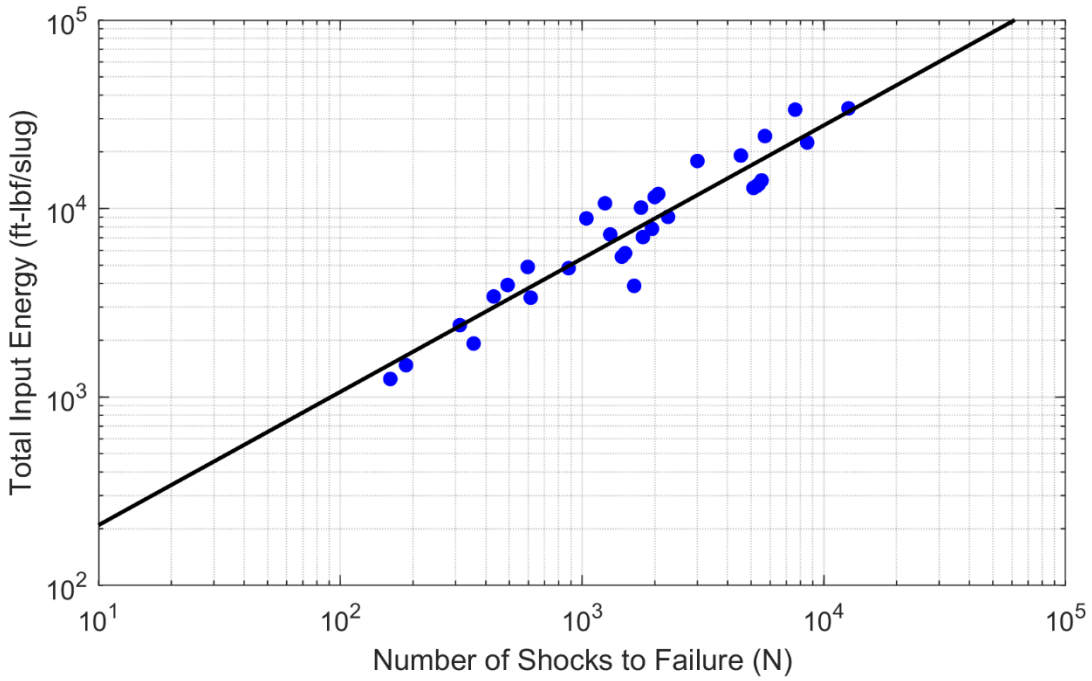


**Figure 41. Plot of Number of Shocks to Failure versus Total Input Energy from SDOF Cantilever Beam Tests in CDL**

Figure 42 shows a plot of the same round beam CDL SDOF fatigue test data formatted to show the number of shocks to failure compared to the average input energy per shock. The slope of the least squares fit straight line through the data is −0.293 which is again very similar to the measured 6-DOF slope of −0.35 and the theoretical slope of −0.36. The apparent striations seen in Figure 42 correspond to the shock levels tested.

Considering that these tests used beams of different cross-sections, manufactured in different lots, tested with a different shock input, on different equipment, the closeness of the results are quite good. Here again, however, the closeness of the results is not the most significant conclusion, rather that the energy again follows the power law relationships like the more common *S-N* results.

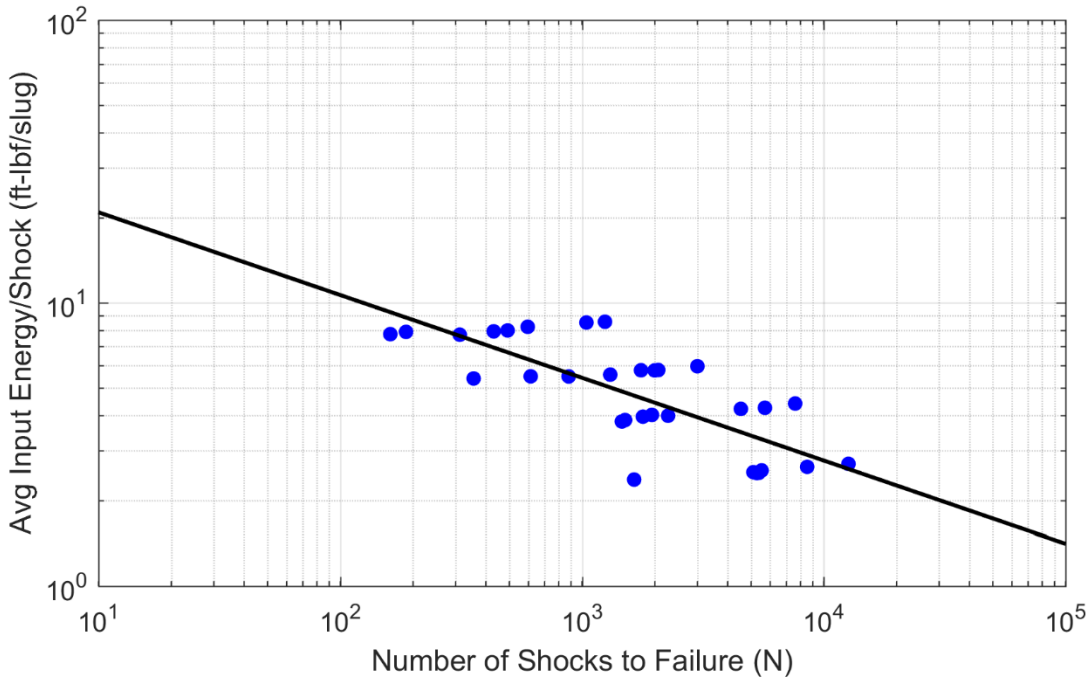


**Figure 42. Plot of Number of Shocks to Failure versus Average Input Energy from SDOF Cantilever Beam Tests in CDL**

# 10. PLATE SHOCK TEST RESULTS

Although the cantilever beam testing was very informative and conducive to verification of the theoretical predictions, it was desired to perform testing on a more complex system. The design of the 3-D printed plate was discussed in Section 5.5. Shock testing of the plate was performed in April and August 2017 in the SNL/NM Mechanical Shock Laboratory on the drop table. A photograph of the plate installed on the drop table for testing is shown in Figure 43. A simple plate test fixture was used for these tests and the plate was supported using printed circuit board stand-offs at two opposing corners as shown.

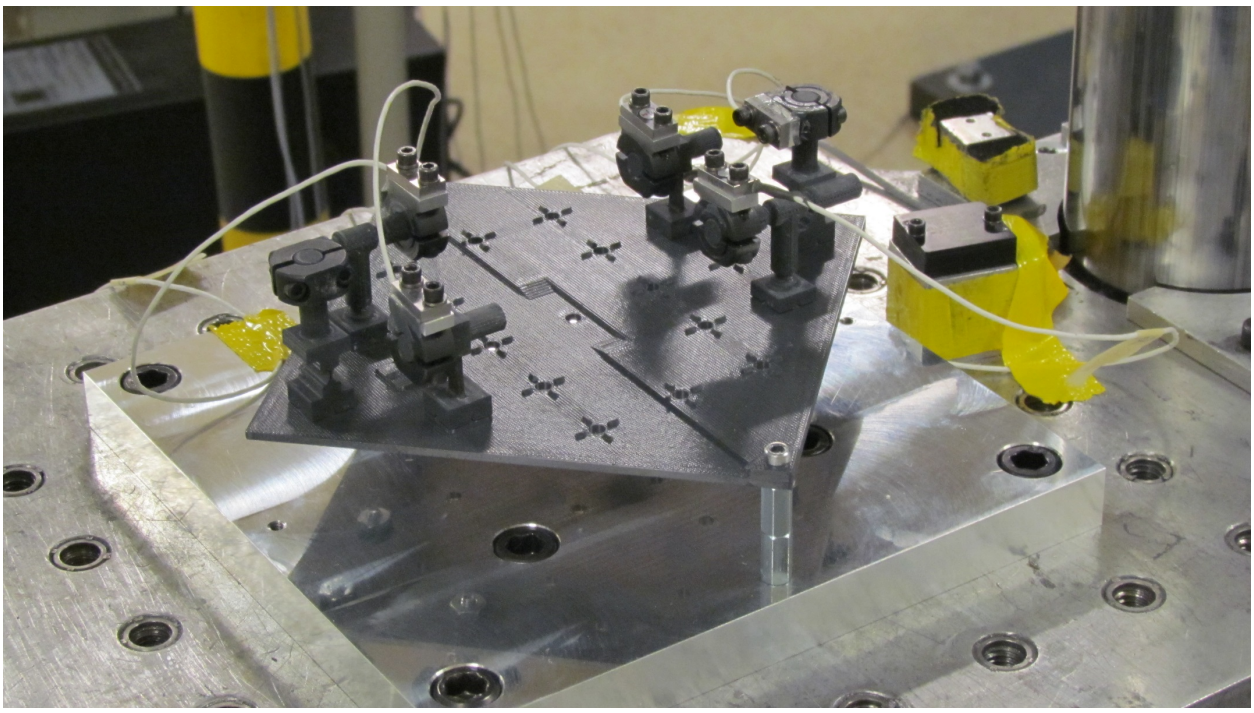

**Figure 43. Plate Structure Installed on the Drop Table for Testing**

Testing was performed in several series. Initial testing focused on increasing the shock level to establish failure points for the various plate components. After this, low-cycle fatigue testing to failure was performed to establish failure versus number of shock curves. Testing was also performed at differing shock pulse durations to alter the spectral content of the applied shock loading. The SRS from two different shock pulses are shown in Figure 44. All tests on the plate structure were performed at a nominal pulse duration of 5 msec or 16 msec although the shock acceleration amplitude was increased or decreased for specific tests.

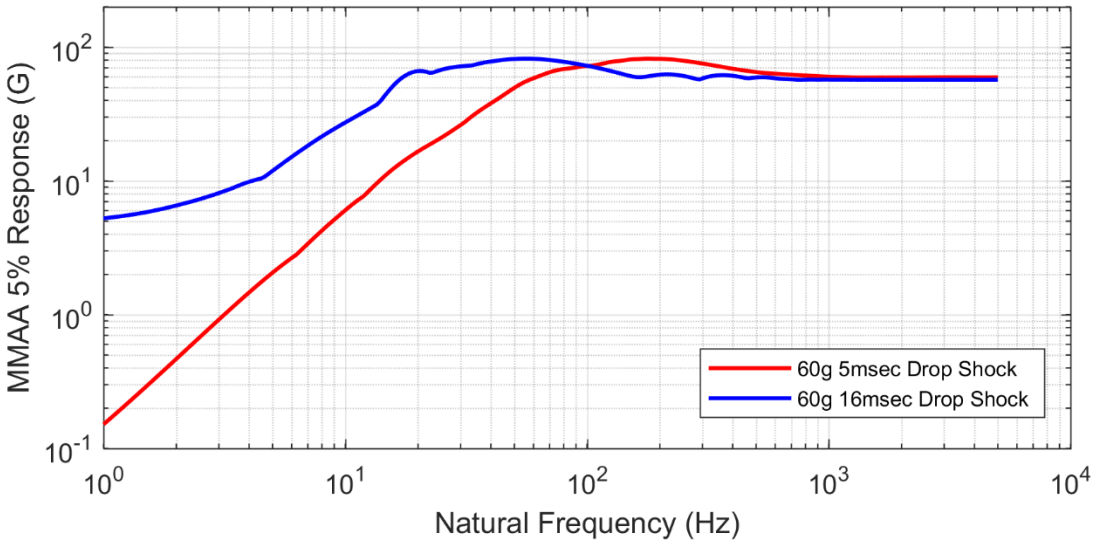


**Figure 44. MMAA SRS from a Nominal Short Duration Shock Pulse and a Nominal Long Duration Shock Pulse**

Figure 45 is a photograph of a typical failure of one of the components on the board. Most failures occurred at the designed-in stress concentration location near the component base as shown here. Most of the components were instrumented for these tests to help understand the response of the components in the system and how the response changed as other components on the plate failed.

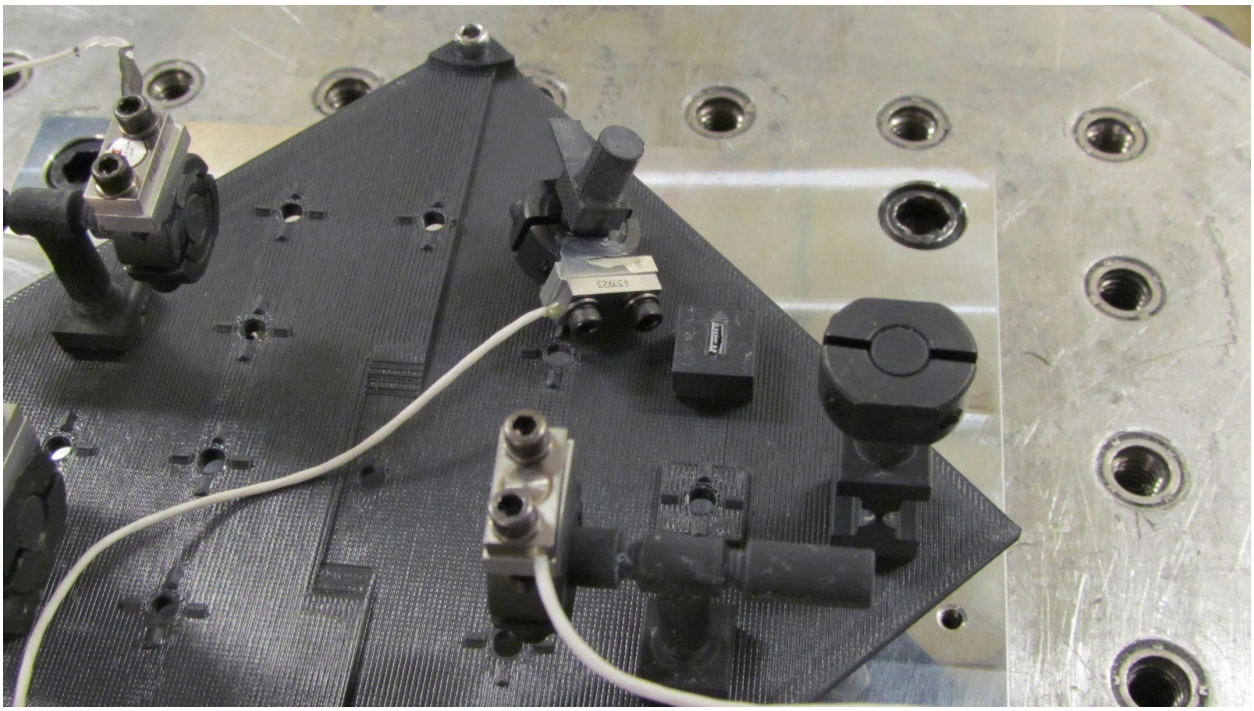

**Figure 45. Sample Component Failure from Drop Table Testing**

In the end, the data from the plate testing proved very difficult to analyze. The testing in April and August did not gather a large enough statistical sample of data to perform the same analysis as was done for the cantilever beams. Additionally, the failures demonstrated much greater variability, perhaps due to the complexity of the structure. Most of the data gathered from these tests will be analyzed further under a subsequent project. However, one set of fatigue data for the small T-Shaped component shown in Figure 45 is presented in Figure 46. Here again, Figure 46 highlights the amount of limited data obtained for some of these components. However, a plot of average specific input energy per shock and number of shocks to failure clearly indicates the logarithmic nature of the fatigue failures. The slope of the least squares fit to the data is −0.33 which is again in-family with the fatigue energy slopes measured from the cantilever beam tests.

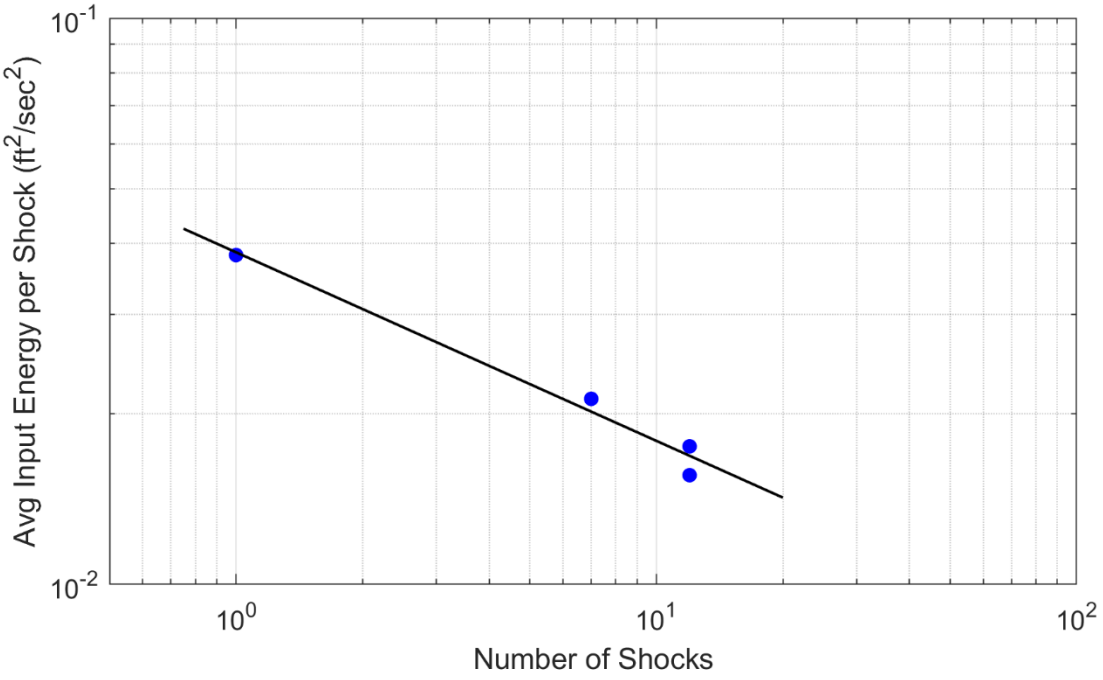


**Figure 46. Fatigue Test Results for the Small T-Shaped Component**

# 11. CONCLUSIONS

The original goal of this WSEAT project was to provide experimental validation for the energy spectra based methods in the context of margin assessment as they relate to shock environments. During this project, a significant number of test articles were designed, manufactured, and tested using different shock machines and shock loads. The results of the extensive testing point to the conclusion, that failure predictions using energy methods as originally defined are not consistent with failure predictions using *S-N* data. While input and dissipated energy accumulate linearly, this linear relationship is not representative of damage accumulation. The test data clearly indicate that input and dissipated energy should have a power law relationship to fatigue damage, with an exponent less than one, if the energy metrics are to be used successfully. As a result, a modification to the energy methods was developed following the form of Basquin's equation to incorporate the material dependent power law exponent for fatigue damage. This update to the energy-based framework brings the energy based metrics into agreement with experimental data and historical *S-N* data.

# 12. REFERENCES


1. Hudson, D. E., "Response Spectrum Techniques in Engineering Seismology," *Proceedings of the World Conference on Earthquake Engineering*, Berkeley, California, 1956, pp. 4.1–4.12.

2. Housner, G. W., "Behavior of Structures During Earthquake," *Journal of the Engineering Mechanics Division (ACSE)*, 1959, Vol. 85, No. 4, pp. 109–129.

3. Zahrah, T. F. and Hall, W. J., "Earthquake Energy Absorption in SDOF Structures," *Journal of Structural Engineering*, Vol. 110, No. 8, August 1984, pp. 1757–1772.

4. Zahrah, T. F. and Hall, W. J., "Seismic Energy Absorption in Simple Structures," *Civil Engineering Studies, Structural Research Series No. 501*, University of Illinois, Urbana, Illinois, July 1982.

5. Edwards, T. S., *Using Work and Energy to Characterize Mechanical Shock*, Technical Report SAND2007–0851J, Sandia National Laboratories, Albuquerque, New Mexico, February 2007.

6. Steinberg, D. S., *Vibration Analysis for Electronic Equipment*, 2nd Edition, John Wiley & Sons, 1988, pp. 275 – 327.

7. MSC Software Corporation*, MSC Nastran 2012 Dynamic Analysis User's Guide*, Santa Ana, California, 2011, pp. 356 – 387.

8. O'Hara, G. J., "Shock Spectra and Design Shock Spectra," NRL Report 5386, 1959.

9. Naval Sea Systems Command, "Shock Design Criteria for Surface Ships," NAVSEA Report 0908-LP-000-3010, Rev. 1, Washington, D.C., 1995.

10. Ordaz, M., Huerta, B., and Reinoso, E., "Exact computation of input-energy spectra from Fourier amplitude spectra," *Earthquake Engineering and Structural Dynamics*, Vol. 32, No. 4, 2003, pp. 597-605.

11. Cheng, P. G., Hecht, T. C., and Bohner, J. J., "Why Satellites Fail: Lessons for Mission Success," Aerospace Report No. TOR-2009(8617)-8704, 2009.

12. Harland, D. M., and Lorenz, R. D., *Space Systems Failures: Disasters and Rescues of Satellites, Rockets and Space Probes*, Springer-Praxis, Berlin, 2005.

13. Edwards, T. S., Power Delivered to Mechanical Systems by Random Vibrations, Shock and Vibration, Vol. 16, No. 3, 2009, pp. 261-271.

14. Scavuzzo, R. J. and Pusey, H. C., *Naval Shock Analysis and Design*, SVM-17, Shock and Vibration Information Analysis Center, 2000.

15. Gaberson, H. A. and Chalmers, R. H., "Modal Velocity as a Criterion of Shock Severity," *Shock and Vibration Bulletin*, No. 40, Part 2, December 1969, pp. 31–49.

16. Edwards, T. S., *W76-0/Mk4 and W76-1/Mk4A Dynamic Environment Capability Study*, SAND2015-7711, Sandia National Laboratories, Albuquerque, New Mexico, September 2015.

17. Lalanne, C., *Fatigue Damage, Mechanical Vibration and Shock Analysis, 3rd Edition*, Vol. 4, John Wiley & Sons, New Jersey, 2014.

18. NASA Technical Handbook, *Dynamic Environmental Criteria*, NASA-HDBK-7005, National Aeronautics and Space Administration, 13 March 2001.

19. SMC Standard SMC-S-16, *Test Requirements for Launch, Upper Stage and Space Vehicles*¸13 June 2008, Section 10.2.2, page 109.

20. Dowling, N. E., *Mechanical Behavior of Materials, Engineering Methods for Deformation, Fracture, and Fatigue, 3rd Edition*, Pearson, Prentice Hall, New Jersey, 2007, page 827-832.

21. International Standard, *Mechanical Vibration and Shock—Signal Processing, Part 4: Shock Response Spectrum Analysis*, ISO 18431-4, 2007

22. Babuška, V., Sisemore, C., and Booher, J., "Energy Based Representations of Mechanical Shock for Design and Environment Characterization," *Proceedings of the 57th AIAA/ASCE/AHS/ASC Structures, Structural Dynamics, and Materials Conference*, San Diego, California, January 2016.

23. Babuška, V., Sisemore, C., and Booher, J., "Mechanical Shock Failure Predictions of a Cantilever Structure Using Energy Response Spectra Methods," *Proceedings of the 86th Shock and Vibration Symposium*, Orlando, Florida, October 2015.

24. Sisemore, C., Babuška, V., and Booher, J., "6-DOF Mechanical Shock Failure Predictions of a Cantilever Structure Using Energy Response Spectra Methods," *Proceedings of the 87th Shock and Vibration Symposium*, New Orleans, Louisiana, October 2016.

25. Sisemore, C., Babuška, V., and Booher, J., "Energy Based Representation of 6-DOF Shaker Shock Low-Cycle Fatigue Tests," *Proceedings of the Society for Experimental Mechanics IMAC XXXV Conference,* Garden Grove, California, January 2017.

# DISTRIBUTION

| | | | |
|---|---|---|---|
| 1 | MS0557 | Greg Tipton | 1522 |
| 1 | MS0557 | Vit Babuška | 1557 |
| 1 | MS0557 | Jerry Cap | 1557 |
| 1 | MS0557 | John Pott | 1557 |
| 1 | MS0557 | Matthew Raymer | 1557 |
| 1 | MS0840 | Jason Booher | 1557 |
| 1 | MS0840 | Carl Sisemore | 1557 |
| 1 | MS0840 | Troy Skousen | 1557 |
| 1 | MS0899 | Technical Library | 9536 (electronic copy) |


Sandia National Laboratories